

# Geochemistry, Geophysics, Geosystems®



## RESEARCH ARTICLE

10.1029/2023GC010992

### Key Points:

- We present an approach to quantify daily growth rates in mollusks with an internal age model based on wavelet transformation of Mg/Ca data
- The resulting highly resolved elemental data versus time can be used to evaluate the timing of (sub) seasonal environmental changes
- The comparison of growth rate and elemental composition in a late-Miocene specimen indicates a (co) dependence of Mg/Ca and growth rate

### Supporting Information:

Supporting Information may be found in the online version of this article.

### Correspondence to:

I. Arndt,  
[arndt@em.uni-frankfurt.de](mailto:arndt@em.uni-frankfurt.de)

### Citation:

Arndt, I., Coenen, D., Evans, D., Renema, W., & Müller, W. (2023). Quantifying sub-seasonal growth rate changes in fossil giant clams using wavelet transformation of daily Mg/Ca cycles. *Geochemistry, Geophysics, Geosystems*, 24, e2023GC010992. <https://doi.org/10.1029/2023GC010992>

Received 7 APR 2023

Accepted 5 SEP 2023

### Author Contributions:

**Conceptualization:** Iris Arndt, Wolfgang Müller

**Data curation:** Iris Arndt




**Formal analysis:** Iris Arndt

**Funding acquisition:** Iris Arndt, Wolfgang Müller

**Investigation:** Iris Arndt, Wolfgang Müller

**Methodology:** Iris Arndt, Douglas Coenen, Wolfgang Müller

## Quantifying Sub-Seasonal Growth Rate Changes in Fossil Giant Clams Using Wavelet Transformation of Daily Mg/Ca Cycles

Iris Arndt<sup>1,2</sup> , Douglas Coenen<sup>1,2</sup> , David Evans<sup>1,2,3</sup> , Willem Renema<sup>4,5</sup>, and Wolfgang Müller<sup>1,2</sup>

<sup>1</sup>Institute of Geosciences, Goethe University Frankfurt, Frankfurt am Main, Germany, <sup>2</sup>Frankfurt Isotope and Element Research Center (FIERC), Goethe University Frankfurt, Frankfurt am Main, Germany, <sup>3</sup>Now at School of Ocean and Earth Science, University of Southampton, Southampton, UK, <sup>4</sup>Marine Biodiversity Group, Naturalis Biodiversity Center, Leiden, The Netherlands, <sup>5</sup>Institute for Biodiversity and Ecosystem Dynamics (IBED), University of Amsterdam, Amsterdam, The Netherlands

**Abstract** Shells of the giant clam *Tridacna* can provide decade-long records of past environmental conditions via their geochemical composition and structurally through growth banding. Counting the daily bands can give an accurate internal age model with high temporal resolution, but daily banding is not always visually retrievable, especially in fossil specimens. We show that daily geochemical cycles (e.g., Mg/Ca) are resolvable via highly spatially resolved laser-ablation inductively coupled plasma mass spectrometry (LA-ICPMS; 3 × 33 μm laser slit) in our Miocene (~10 Ma) specimen, even in areas where daily banding is not visually discernible. By applying wavelet transformation on the measured daily geochemical cycles, we quantify varying daily growth rates throughout the shell. These growth rates are thus used to build an internal age model independent of optical daily band countability. Such an age model can be used to convert the measured elemental ratios from a function of distance to a function of time, which helps evaluate paleoenvironmental proxy data, for example, regarding the timing of sub-seasonal events. Furthermore, the quantification of daily growth rates across the shell facilitates the evaluation of (co)dependencies between growth rates and corresponding elemental compositions.

**Plain Language Summary** Shells of giant clams exhibit growth bands, similar to tree rings, which form in both seasonal (visible by eye) and daily (resolvable by microscope) increments. However, the optical visibility of daily bands in fossil giant clam shells can be poor. Fortunately, growth bands are often accompanied by changes in the chemical composition of the shell. The incorporation of trace elements into the shell depends on environmental factors (like temperature and light) and biological controls, which are both characterized by cyclic daily variation. With our Python script *Daydacna*, we present a tool that enables daily resolution scale changes in growth rate to be evaluated using daily geochemical cycle lengths, that is, how much the shell has grown each day. *Daydacna* then creates an internal age model and converts the respective element compositions from being expressed over distance to being expressed over time. This information enables an unambiguous estimate of growth rate to be compared to elemental compositions, enabling (e.g.) potential (co) dependencies of these parameters to be identified. Time-resolved data also allow to determine the timing of seasonal environmental changes, affecting the shell composition, with higher confidence and thus form an important basis for research on the seasonal aspects of the (paleo)climate.

## 1. Introduction

*Tridacna* (giant clams) provide decades-long, sub-daily resolvable archives of (sub)tropical reef environments. Specifically, by analyzing the geochemical composition of their aragonitic shells, environmental parameters can be reconstructed, such as temperature (e.g., Ayling et al., 2015; Batenburg et al., 2011; Pätzold et al., 1991), light availability (e.g., Hori et al., 2015; Warter et al., 2018) and nutrient availability (Arias-Ruiz et al., 2017; Batenburg et al., 2011; Elliot et al., 2009) as well as short-term disturbances of reef systems, such as storms and heavy precipitation events (Komagoe et al., 2018; Yan et al., 2020). *Tridacna* emerged in the early Miocene (Harzhauser et al., 2008) and are mostly mixotroph organisms (Jantzen et al., 2008), feeding on glucose produced by their photosymbionts and filtering particulate nutrition from the environment (Kunzmann, 2008). Their ability to record both seasonal variability and short-term events as well as the excellent fossilization potential of their large dense aragonitic shells make them well-suited paleoclimate archives even in “deep-time” (Batenburg et al., 2011; Harzhauser et al., 2008;

© 2023 The Authors. *Geochemistry, Geophysics, Geosystems* published by Wiley Periodicals LLC on behalf of American Geophysical Union. This is an open access article under the terms of the [Creative Commons Attribution License](https://creativecommons.org/licenses/by/4.0/), which permits use, distribution and reproduction in any medium, provided the original work is properly cited.

**Project Administration:** Wolfgang Müller  
**Resources:** Willem Renema, Wolfgang Müller  
**Software:** Iris Arndt, Douglas Coenen  
**Supervision:** David Evans, Wolfgang Müller  
**Validation:** David Evans, Wolfgang Müller  
**Visualization:** Iris Arndt  
**Writing – original draft:** Iris Arndt  
**Writing – review & editing:** Iris Arndt, Douglas Coenen, David Evans, Wolfgang Müller

Warter et al., 2015). As seasonality is an important component of the climate system, seasonally resolved data greatly help in constraining palaeoclimate reconstructions and may be used to test the skill of climate models (Carré & Cheddadi, 2017; Cauquoin et al., 2019; Schmidt et al., 2014; Tierney et al., 2020).

Besides geochemical variability, macro and microstructures within the shell reflect changes in the environmental setting of clams (Gannon et al., 2017). *Tridacna* shells feature seasonal (macroscopically visible at mm scales) to daily (microscopically visible at  $\mu\text{m}$  scales) growth bands. Daily growth bands can be counted to determine time intervals within recent giant clams (Duprey et al., 2015; Gannon et al., 2017; Sano et al., 2012; Zhao et al., 2023). However, microscopic daily growth band visibility is not always sufficient for reliable counting, especially in fossil shells (Figure 1e, Figures S1 and S2 in Supporting Information S1; Section 3.2).

Alternatively, seasonal bands at the macroscale or annual cycles in the oxygen isotopic composition of the shell ( $\delta^{18}\text{O}$ ) have been used to determine the ontogenetic age of fossil giant clams and to evaluate seasonal and multiannual paleoenvironmental changes (Ayling et al., 2015; Batenburg et al., 2011; Driscoll et al., 2014; Warter et al., 2015). However, in many tropical areas, seasonality is manifested not via large temperature variability but rather via substantial changes in precipitation, which may complicate the interpretation of  $\delta^{18}\text{O}$  records obtained from *Tridacna* specimens and their usability for indicating yearly time intervals (Ma et al., 2020). This argues for either an alternative macro-scale geochemical proxy or a reliable micro-scale analysis of the shell. Fortunately, it is possible to measure daily increments within fossil *Tridacna* shells via spatially resolved geochemical analysis. Analytical methods suitable for resolving daily changes in elemental composition are (Nano) Secondary Ion Mass Spectrometry (e.g., Füllenbach et al., 2017; Hori et al., 2015; Sano et al., 2012; Yan et al., 2020), Electron Probe Micro Analyzer measurements (Füllenbach et al., 2017; Hori et al., 2015), and Laser-Ablation Inductively Coupled Plasma Mass Spectrometry (LA-ICPMS) (e.g., Warter & Müller, 2017; Warter et al., 2018). LA-ICPMS is a more rapid and inexpensive method (Warter & Müller, 2017) and may therefore be advantageous in determining the ontogenetic ages of large (100–1,000 mm) and long-lived *Tridacna* shells by daily band analysis.

Here we present a method applicable to the rapid generation of a reliable internal age model for fossil (*Tridacna*) shells. Specifically, we show that daily resolved internal age models can be generated by assessing the changing wavelengths of daily cycles of elemental ratios (e.g., Mg/Ca) measured via high resolution LA-ICPMS. We demonstrate the suitability of this approach for assessing paleo-seasonality by enabling high-resolution analysis of geochemical parameters over time rather than shell distance. Time resolved paleoenvironmental proxy data can be compared seasonally, which improves the interpretation of reoccurring seasonal environmental changes. Additionally, we aim to further our understanding of the relationship between growth rate and geochemical proxies. Comparing the daily resolved growth rate changes to geochemical data helps decipher growth rate dependent and independent proxy variability.

In general, the approach developed here is not only applicable to *Tridacna* but also to other organisms and archives providing cyclic data sets (see Section 5).

## 2. Materials and Methods

### 2.1. Sample Origin and Preparation

A large fossil *Tridacna* sample (TOBI; Figure 1a) was sampled in East Borneo in early November 2013, near Bontang ( $0^{\circ}08'15''\text{N}$ ,  $117^{\circ}26'21''\text{E}$ ). The shell was recovered from a micritic bioclast packstone horizon within silty shales and sandstones (Renema et al., 2015). Other bivalve shells and corals from the “Bontang Garden” location have been dated via Strontium Isotope Stratigraphy, suggesting that fossils from this location can be assigned to the Tortonian (late Miocene) (Renema et al., 2015).

The shell was externally cleaned with a brush, rinsed with tap water and dried before being cut along its maximum growth axis. The central slab was divided into smaller rectangular slabs ( $55 \times 28 \times 7$  mm) with slightly overlapping areas (Figure 1a). From the slabs, thin sections of 50  $\mu\text{m}$  thickness were cut using a G&N MP2 2R 300 surface grinder and polished with 3  $\mu\text{m}$  diamond suspension on a Logitech PM2A. These thin sections were used for both imaging (e.g., Figures 1c–1f) and LA-ICPMS analysis.

### 2.2. Microscope Imaging

In order to obtain information on the shell structure, microscope images of the polished thin sections were taken using a Keyence VHX-6000 microscope with full ring incident light. For overview images we used 20 $\times$  magnification,

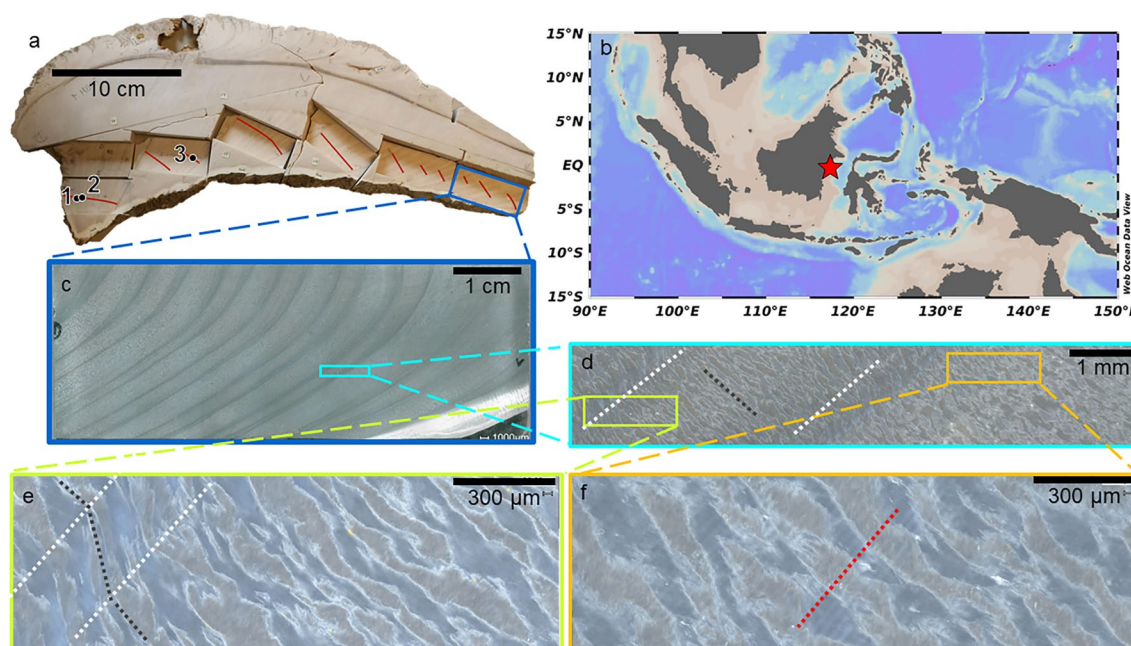


**Figure 1.** (a) Cross section of the late Miocene *Tridacna* shell (TOBI) with six slabs cut for analysis. The numbered points refer to the position of the three laser-ablation tracks presented and discussed in this paper. (b) Ocean Data View map of the Indo-Pacific region with the sampling location marked by a star. (c) Thin section of the ontogenetic oldest slab with presumably semi-seasonal dark banding. (d) Close-up of c with crossed lamellar crystal structure striking at an angle of  $\sim 135^\circ$  (dark gray dotted line) and two dark bands striking at an angle of  $\sim 45^\circ$  (white dotted lines). (e) Close-up of d, showing the crossed lamellar crystal structure within part of a dark band. These brownish and grayish structures likely reflect aragonite crystals of different orientations. The angle of the crystal structure changes around the dark banding, from around  $135^\circ$  to around  $110^\circ$ . (f) Close-up of d, with crossed lamellar crystal structure and daily banding striking at an angle of  $\sim 45^\circ$  (red dotted line).

areas around the high-resolution laser-ablation (LA) tracks were documented at  $400\times$  magnification, and pictures up to  $2000\times$  magnification were taken of areas of specific interest, for example, within dark presumably semi-seasonal bands. Where possible, daily bands were counted (Figures S3 and S4 in Supporting Information S1) and a semiquantitative analysis of daily band widths in different areas of the shell was conducted by counting daily increments over distance.

### 2.3. Phase Assessment via Attenuated Total Reflectance Fourier Transform InfraRed Spectrometry (ATR-FTIR) and X-Ray Diffractometry (XRD)

Material from the rim of the shell was sampled using a handheld slow-rotating diamond-tipped drill. From the inner shell, the material was cut out with a diamond blade saw and powdered by hand using an agate mortar. This procedure was chosen to avoid any recrystallization of aragonite to calcite during the drilling process, as previously observed (Aharon, 1991; Foster et al., 2008). The mineralogical composition of the powder samples was measured both by XRD, namely a PANalytical X'Pert PRO X-ray diffractometer, equipped with a copper X-ray tube and a Ni-filter, and by ATR-FTIR, namely a Bruker Alpha II equipped with a diamond ATR attachment. ATR-FTIR baseline subtraction was performed using a baseline measurement (12 scans) taken immediately prior to sample data acquisition (24 scans), while data were collected between  $350$  and  $4,000\text{ cm}^{-1}$  at a resolution of  $4\text{ cm}^{-1}$ .

### 2.4. LA-ICPMS

LA-ICPMS analysis was carried out using a RESolution LR laser-ablation system equipped with a two-volume S155 cell (Laurin Technic; Müller et al., 2009) coupled to a ThermoScientific Element XR sector field mass spectrometer. Prior to analysis, thin sections were ultrasonically cleaned using ethanol.

Ablation took place in He atmosphere, with Ar added at the top of the funnel, and  $\text{N}_2$  admixed downstream of the cell at  $\sim 4\text{ ml/min}$ . Tuning was performed using a  $60\text{ }\mu\text{m}$  spot, with  $1\text{ }\mu\text{m/s}$  scan speed and  $5\text{ Hz}$  repetition rate. Following Warter et al. (2018), ablation was carried out using a rotatable rectangular laser slit. Here, we use a  $3 \times 33\text{ }\mu\text{m}$  slit, which has an ablation surface area similar to a  $15\text{ }\mu\text{m}$  circular spot, hence yielding equivalent ICPMS signal intensities. All laser tracks were set parallel to the maximum growth axis, that is, orthogonal to

**Table 1**

*Results of Standard Reference Materials Measured Using the  $3 \times 33 \mu\text{m}$  Slit Compared With Reference Values for MACS-3 (Na, Mg, Sr, Ba: Solution Based USGS-Data From Stephen Wilson (Pers. Comm, 2010); B: Laser-Ablation Inductively Coupled Plasma Mass Spectrometry Data With Medium Mass Resolution and 193 nm Wavelength; Jochum et al., 2012) and KL2-G (GeoReM Preferred Values; Jochum et al., 2006); Accuracy and External Precision for Each Element*

		Measured mean ( $\mu\text{g/g}$ ) $\pm$ 2 SD	Reference value ( $\mu\text{g/g}$ ) $\pm$ 2 SD	Accuracy (%)	Precision (% 2 RSD)
B	MACS-3	10.13 $\pm$ 1.84	8.9	13.82	18.13
	KL2-G	2.88 $\pm$ 0.40	2.73 $\pm$ 0.28	5.49	13.73
Na	MACS-3	7,711 $\pm$ 1,053	5,900 $\pm$ 800	30.70	13.66
	KL2-G	17,051 $\pm$ 544	17,434 $\pm$ 593	-2.20	3.19
Mg	MACS-3	1,948 $\pm$ 108	1,756 $\pm$ 272	10.91	5.55
	KL2-G	43,519 $\pm$ 1,296	44,263 $\pm$ 543	-1.68	2.98
Sr	MACS-3	7,205 $\pm$ 238	6,760 $\pm$ 700	6.58	3.31
	KL2-G	355 $\pm$ 8	356 $\pm$ 8	-0.28	2.34
Ba	MACS-3	77.3 $\pm$ 7.2	58.7 $\pm$ 4.0	31.70	9.31
	KL2-G	127 $\pm$ 2	123 $\pm$ 5	3.25	1.50

the daily bands. Precleaning took place at 7  $\mu\text{m/s}$  scan speed and 20 Hz repetition rate, while measurements were conducted at a scan speed of 1  $\mu\text{m/s}$  and 10 Hz repetition rate. We monitored the isotopes  $^{11}\text{B}$ ,  $^{23}\text{Na}$ ,  $^{24}\text{Mg}$ ,  $^{27}\text{Al}$ ,  $^{43}\text{Ca}$ ,  $^{88}\text{Sr}$ ,  $^{89}\text{Y}$ , and  $^{138}\text{Ba}$ , with a total sweep time of 330 ms, resulting in a sampling frequency of  $\sim 0.34 \mu\text{m}$ . We do not further present or discuss  $^{27}\text{Al}$  data as they lie largely below the limit of detection.  $^{89}\text{Y}$  data were measured to check any possible diagenetic alternation and are, like  $^{27}\text{Al}$ , only displayed with the full data set in Figure S5 of Supporting Information S1. Instrumental tuning was performed on the standard reference material NIST SRM 612. The plasma was tuned to a  $\text{ThO}^+/\text{Th}^+$  rate of 0.4%, a Th/U ratio of 0.97, and a normalized argon index (Fietzke & Frische, 2016) of 1.1, while double-charged production at 1.5% was monitored via the 22/44 ratio. At 10 Hz, we did not use the signal smoothing squid in order to maximize the spatial resolution (Müller et al., 2009). An overview of the measurement and tuning parameters can be found in Table S1 of Supporting Information S1.

Element/Ca (El/Ca) ratios were calibrated using NIST SRM 612 as the bracketing external standard (Jochum et al., 2011) with updated Mg values (Evans & Müller, 2018) and  $^{43}\text{Ca}$  as the internal standard. Data quantification follows Longerich et al. (1996) and was performed using the software Iolite 4 (Paton et al., 2011). Data quality (accuracy and precision) was determined by measuring the MPI-DING glass KL2-G (Jochum et al., 2006) and the nanopellet carbonate standard MACS-3NP (Garbe-Schönberg & Müller, 2014) treated as unknowns and analyzed in the same way as the samples; data are shown in Table 1.

Further data evaluation and visualization was done using Python and facilitated through the use of the Python libraries and packages NumPy (Harris et al., 2020), Pandas (Reback et al., 2022), and Matplotlib (Caswell et al., 2022) as well as PyCWT based on Torrence and Compo (1998).

## 2.5. Wavelet-Analysis: New Python Script “Daydacna”

### 2.5.1. Data Pre-Treatment

Prior to further analysis, we removed outliers from the data set. Because the data are both cyclic and display long-term trends, we detrended the data before determining outliers. Detrending was conducted by subtracting a 20-point running mean from the original signal to remove most underlying variability. Subsequently, all data points outside the two standard deviation range were selected as outliers. These data points were excluded from the original data set and replaced with linearly interpolated values. Rejecting data points over two standard deviations resulted in a clearer signal and less noisy wavelet scalogram compared with rejecting only points over three standard deviations.

### 2.5.2. Continuous Wavelet Transform (CWT) Basics

To evaluate the wavelength shifts within the daily El/Ca cycles, we applied CWT (Goupillaud et al., 1984) to the data set. In CWT, an input function is multiplied by a wavelet. The wavelet used in this study is a real-value Morlet wavelet (Morlet et al., 1982). This wavelet is continuously scaled and shifted in its position within a given range.

The product of wavelet and input function is integrated, and the resulting coefficient can be used to determine the correlation between wavelet and input function at a given frequency, including the position of the wavelet.

The resulting correlation between the wavelet and input function at a given interval and a given frequency of the wavelet was used to determine the main frequency present in the input for said interval. The continuous shift in location and frequency of the wavelet during its comparison to the input data allows for the analysis of shifts in frequency over distance within the input data set itself. This is best visible in a scalogram in which the relative correlation intensity is displayed in color with distance or time on the  $x$ -axis and wavelength on the  $y$ -axis (e.g., Figure 2). In our new data evaluation script “*Daydacna*,” we use the Python package PyCWT (based on Torrence and Compo (1998)) to calculate and display our CWTs.

### 2.5.3. Wavelet Correlation Maxima and Growth Rate Evaluation

Figures 2a–2d illustrate the steps taken by the *Daydacna* script. We apply a combination of automated maxima detection, manual correction, and smoothing to determine the wavelengths of daily cycles, hence directly translating to daily growth rates. These form the basis for the estimation of the number of days included in the data set. We use a Monte Carlo approach to quantify the uncertainty of this estimation.

As a first step, the frequencies with the maximum correlation coefficient at a given point over distance are selected to determine the main frequency within the input data (red lines, Figure 2a). Here, we set the maximum limit for detection to 40  $\mu\text{m}$  because daily band widths were optically determined to be 38  $\mu\text{m}$  or below throughout the shell (see Section 3.2). In step two, an initial interpolation and locally weighted scatterplot smoothing (LOWESS) statistical regression function based on Cleveland (1979) using the statsmodels Python module (Seabold & Perktold, 2010) is applied to smooth through the correlation maxima detected in step one (black line, Figure 2b). Overlying lower frequencies can at times show a clearer cyclicity in the data set and therefore have higher correlations than daily cycles. Thus, the dominant wavelengths highlighted by *Daydacna* in the resulting graph may not always represent daily cycles. To correct this issue, we implemented a mixture of automatic and manual adjustments. In areas where overlying (greater than daily) frequencies dominate over longer distances, manual readjustment of the pathway might be necessary. The user can choose a more likely pathway for such areas by selecting other points of high correlation (blue dots, Figure 2b). These manually set points within one pathway are in turn connected linearly (blue lines, Figure 2b), which overall replaces the automatically detected pathway in that data range. A Monte Carlo approach was used to account for the uncertainty of manually selecting the approximate area of high correlation related to the daily signal. Both  $x$  (distance) and  $y$  (wavelength) values of each manually selected point are randomly selected (1,000 times) from a normal distribution using the point's coordinates as mean and 1% of the mean value as the standard deviation. In a third step, maxima will be reselected automatically, but this time only close to the pathway describing the approximate area in which the daily signal is expected based on Monte Carlo simulations. The upper and lower boundaries of the range in which maxima are selected are also determined by a Monte Carlo simulation with 1,000 iterations. The mean of the upper and lower boundaries is centered on the smoothed pathway plus or minus 0.5  $\log_2$  units respectively. Based on these mean values, the boundaries are randomly sampled from a normal distribution with a standard deviation of 0.05 ( $\sim 10\%$  uncertainty). The smoothed pathway is processed as  $\log_2$  of the selected wavelengths; therefore, the range of interest is displayed uniformly across the scalogram (Figure 2c). Correlation maxima detected outside the area of interest, that is, far away from the smoothed detected pathway, are automatically excluded in this second maxima detection step (Figure 2c). Through microscope observations, we found that growth rate changes are rather gradual (see Section 3.2, Results). Therefore, we created smoothed pathways through the detected maxima in the last step. Here we use a convolution algorithm for each of the 1,000 envelopes, rather than smoothing with LOWESS, because the computational time needed for the latter is more than three orders of magnitude higher, making it unsuitable for Monte Carlo simulations on large data sets. However, the convolution algorithm has boundary effects, impacting the rim domains from a distance equivalent to half of the smoothing window. We cannot properly assess the uncertainty introduced by smoothing in these rim areas, but since they make up only about 3% of the entire data set, we consider this contribution to be minor. The smoothing window span is also simulated in 1,000 iterations using a Monte Carlo approach. Here, we chose a mean smoothing window span of 400 data points with a standard deviation of 75. The resulting 50th percentile pathway describes the changes in wavelengths over distance (dashed line, Figure 2d) and the 2.5th and 97.5th percentiles are used to represent the uncertainties (indicated in gray, Figure 2d). Because of the aforementioned steps, different thresholds, and working with linear and  $\log_2$  scales, the resulting array of Monte Carlo simulated number of days in the sample is not always normally distributed. As such, we use the 2.5th/97.5th percentiles in addition to the 2 SD values.

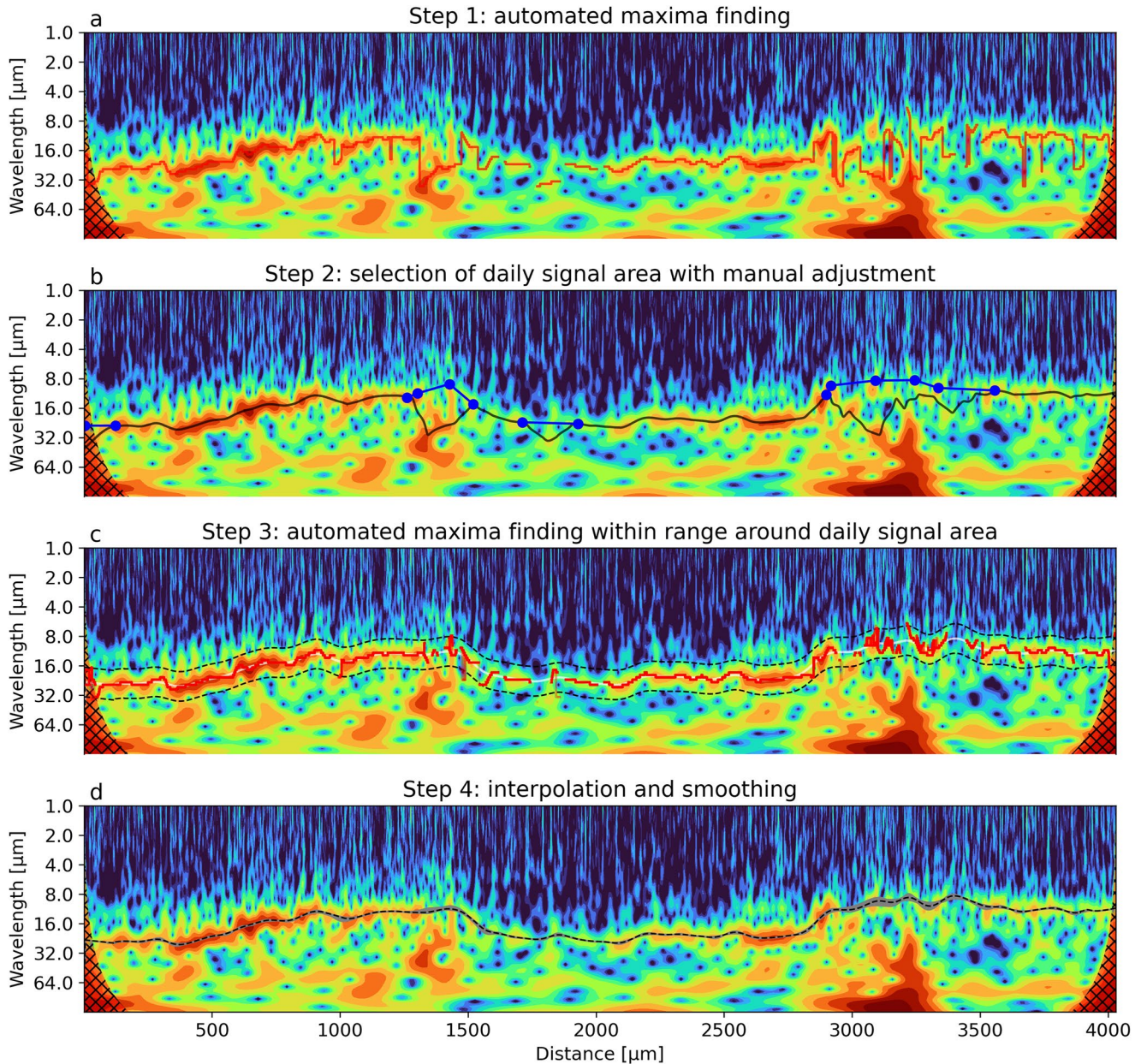


**Figure 2.** Steps performed by the *Daydagna* script to assess the daily growth rate from the continuous wavelet transform (CWT) scalogram of the Mg/Ca data set of LA track 2 (for details see Section 3.3.2, Figure 4). The y-scale is inverted and on a log<sub>2</sub> scale. (a) Step 1: Correlation-maxima are selected within the range of potentially occurring daily cycles (up to 40  $\mu\text{m}$ , based on observation). (b) Step 2: If these maxima are unlikely to represent daily cycles (criteria see Sections 2.5.3 and 4.2), an alternative area of interest can be selected manually, indicated in blue. (c) Step 3: An area of interest is defined around a smoothed curve of the selected maxima and areas of manual correction excluding outliers and artificial jumps in growth rate. The black dashed lines indicate the 50th percentile of the Monte Carlo simulated area of interest. Correlation maxima are detected for a second time but now only within the area of interest (red domains). In this way, low frequency overlying signals with higher correlations than the daily signal are excluded. (d) Step 4: The maxima are interpolated and smoothed with different smoothing window spans via Monte Carlo simulation. The 50th percentile curve, which is used to determine growth rates over distance, is indicated as the black dashed line. Confidence intervals (2.5th and 97.5th percentiles;  $\sim 2$  SD) are displayed by the area shaded in gray.

Our time series analysis approach provides a data set of wavelengths over distance, which traces the lengths of the daily El/Ca cycles recorded within the shell. The wavelength of each daily cycle represents the shell growth per day along the measured transect. With the smoothed growth rate pathway, we can quantify the growth rate in  $\mu\text{m}$  per day for each given point, which allows us to quantify the time represented between two data points as a fraction of a day. The cumulative sum of time between data points over distance along the shell results in an internal age model based on daily growth rates. This allows us to obtain an overall estimate of the number of days included

in the measured LA track and quantify the distribution of time over distance. In order to assess and quantify the uncertainties associated with the determination of days in a data set, we modify—via Monte Carlo simulations—the parameters used to establish the daily growth rate, which have to be set but are difficult to determine. These factors include the exact position of the high correlation area attributed to daily cyclicity by manual selection, the range of area of interest around the approximate pathway of daily wavelengths and the smoothing window span.

Ultimately, we apply the internal age model derived as described above to display the measured data against time rather than distance. When doing so, data points plotted versus time are no longer evenly spaced, in contrast to plotting against distance. Nonetheless, this provides a test of the model as the daily cycles should all be displayed as being equally long on the time scale (1 day).

### 3. Results

#### 3.1. Preservation of the Shell

While the outer rim (~1 cm) shows visible alteration, characterized by a change in color and at times visible recrystallization, the inner part of the shell has an optically pristine appearance as it displays no signs of recrystallization or dissolution (Figure 1c). The original crystal structure is well preserved and visible in the microscope images (Figure 1d–1f). Furthermore, the EI/Ca ratios (see below) are very similar to those of modern *Tridacna* shells (Batenburg et al., 2011; Sano et al., 2012; Warter et al., 2018). The measured Y/Ca ratios do not indicate diagenetic alteration (Figure S5 in Supporting Information S1). XRD and ATR-FTIR measurements confirm that the aragonite is preserved throughout the bulk of the shell analyzed here, whereas both calcite and aragonite are detected in the powder samples from the outermost rim (Figures S6 and S7 in Supporting Information S1).

#### 3.2. Optical Analysis of Presumably (Sub)seasonal and Daily Bands

Along the cross-section of the shell, a conspicuously regularly occurring light-dark banding pattern is visible (Figures 1a and 1c). The banding pattern may be irregular, but especially in the ontogenetically older area of the shell, a double-banding structure prevails (Figure 1c). In areas where daily bands are visually resolvable, we could count around 70–100 days between the centers of the two bands close to each other, while the larger gaps usually contain more than 200 days. This indicates that the macroscopically visible dark bands in our sample are likely to be produced seasonally.

The various microscopy techniques applied did not unequivocally resolve the daily bands throughout the shell. In some areas of the shell daily bands are well resolvable with 400× magnification. In areas where daily bands are not visible in 400× magnification, a five-fold increase in magnification generally did not result in better daily band discernibility. We further unsuccessfully tried to enhance daily band visibility by treating slabs and thin sections with Mutvei's solution, as described in Schöne et al. (2005), prior to microscopic assessment and imaging (Figure S8 in Supporting Information S1). In order to enhance the visibility of daily growth bands in recent specimens, fluorescence microscopy has been utilized, which triggers the autofluorescence of the organic content within the shell, which varies on a daily scale (Duprey et al., 2015; Ma et al., 2020; Yan et al., 2020). Our fossil sample did not, however, display distinct continuous daily banding via fluorescence microscopy (Figure S9 in Supporting Information S1). Furthermore, daily bands were not distinguishable via Scanning Electron Microscope imaging, nor did their density difference allow them to be distinguished using  $\mu$ CT or via X-ray imaging (Figure S10 in Supporting Information S1). Daily geochemical EI/Ca cycles, however, are preserved and resolvable in areas where the microscopic bands were not well visible in our fossil specimen (Figure S1 in Supporting Information S1).

The daily band visibility is slightly better in the ontogenetically youngest part of the shell, where the daily bands are widest with a maximum of 38  $\mu$ m. However, daily band visibility and the lack thereof are not directly coupled to ontogenetic age. Rather, there are bands and patches in which visibility is better or worse throughout the shell section. In areas with good daily band visibility, we observed the following recurring patterns. We found that daily band widths decrease towards the macroscopically visible dark (more translucent) presumably seasonal bands. Daily band widths further decrease within the dark bands to well below 10  $\mu$ m and at times below 5  $\mu$ m with a minimum of 2  $\mu$ m. A gradual increase in daily band width is seen at the end of the dark band until a relatively constant daily band width is reached in the lighter (less translucent) parts of the shell (e.g., Figure S4 in Supporting Information S1). The observation of reduced widths of the microscopically visible daily growth bands within the macroscopically visible darker presumably seasonal bands holds throughout the shell, linking the dark

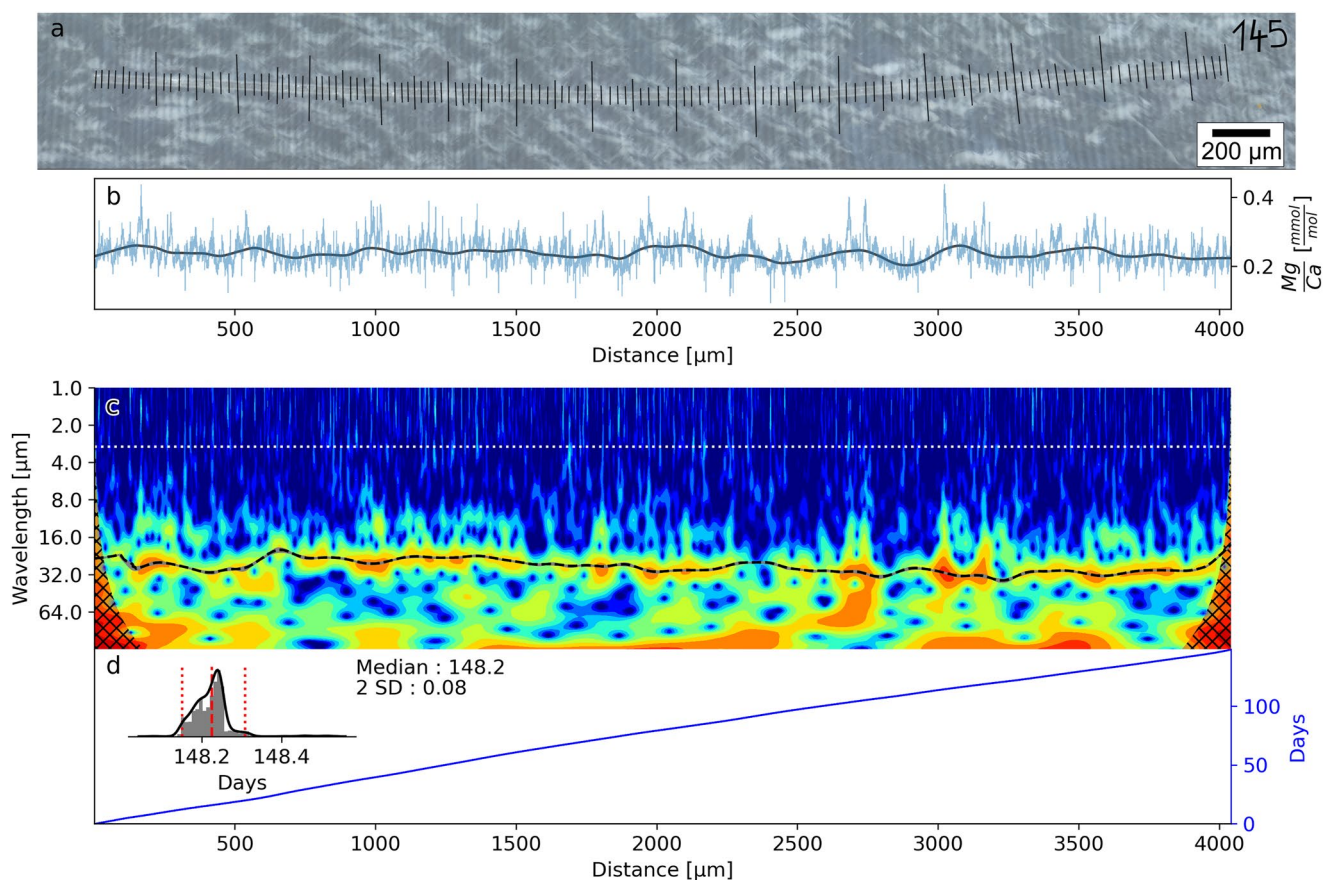


**Figure 3.** (a) Microscope image along LA track 1. Daily bands are visible and counted to be 145 full bands (highlighted in black). (b) Measured Mg/Ca (light blue) from the same track versus distance with resolvable daily cyclicality, with locally weighted scatterplot smoothing curve smoothed over 600 data points shown in gray. (c) Continuous wavelet transform scalogram of the Mg/Ca signal with determined growth rates over distance (dashed line). (d) Internal age model indicating the range of number of days across distance. The overall number of days  $\pm$  2 SD determined from daily Mg/Ca cycles by our *Daydacna* script is  $148.2 \pm 0.08$  with an offset of 3 days (2%).

bands to reduced growth of the organism. The crossed lamellar aragonite crystal structure (Figure 1e–1g) shows a steepened angle within the dark low growth bands (Figure 1e).

Daily bands were counted along LA tracks in areas with good daily band visibility. A comparison of the counted numbers of daily bands and Mg/Ca cycles confirmed their 1:1 relation. The counted sections also provide a basis for checking the accuracy of the age estimates generated via our wavelet-analysis-based Python script *Daydacna* (see Section 3.3).

### 3.3. LA-ICPMS Data, Growth Rate, and Internal Age Model

In the following, we present the results for three LA tracks. We chose to run *Daydacna* on the Mg/Ca rather than Sr/Ca data sets, because the daily cycles were more clearly expressed in Mg/Ca (compare Figure 3 and Figure S11 in Supporting Information S1). The first LA track is from an area of relatively uniform growth within the shell. The daily bands corresponding to the measurements were countable (Figure 3). The second track includes two dark presumably seasonal bands with reduced growth. Along this track, the daily bands were also countable (Figure 4). The third one includes four dark bands and is situated in an area where continuous counting of growth bands was not possible (Figure 5).

#### 3.3.1. Track 1: Uniform Growth and Optically Countable Daily Bands

Along the first LA track, 145 daily bands were optically counted (Figure 3a). The daily bands are relatively evenly spaced in the microscope image. Mg/Ca values range from 0.09 to 0.44 mmol/mol with a mean of 0.24 mmol/mol.



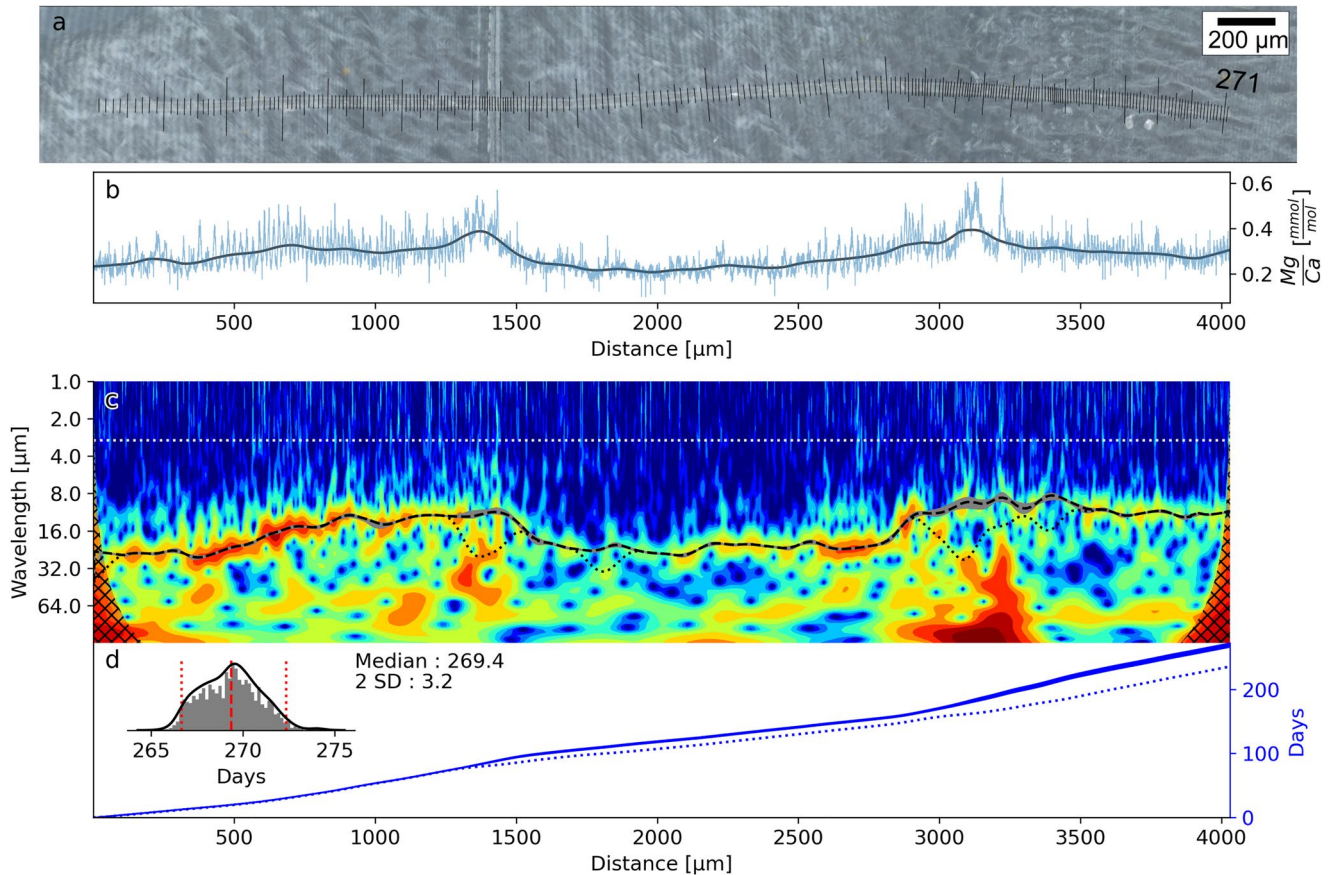


**Figure 4.** (a) Microscope image along LA track 2. Daily bands are visible and indicate that this LA track includes 271 days. (b) Measured Mg/Ca (light blue) from LA track 2 versus distance, with daily cycles at times too narrow to be resolvable at the overview scale. The 600-point locally weighted scatterplot smoothing curve (gray) shows a long-term trend with two maxima around 0.4 mmol/mol, coinciding with areas with narrow daily banding in panel a. (c) The continuous wavelet transform scalogram of the Mg/Ca signal shows variability in the determined growth rates with manual correction (dashed line). The 2.5th/97.5th percentile ( $\sim 2$  SD) is displayed by an area shaded in gray. The pathway without manual correction is displayed by a dotted line. (d) The internal age model (days vs. distance in blue) reflects the non-linear growth rates determined. The thickness of the blue curve reflects the 2.5th to 97.5th percentile interval, also displayed by red dotted lines in the inserted distribution graph. The overall number of days  $\pm 2$  SD determined from the Mg/Ca signal for LA track 2 is  $269.4 \pm 3.2$ . The offset of days counted versus determined by *Daydacna* is 2 days (0.7%). The blue dotted line represents the uncorrected age model.

The overall rather flat LOWESS curve, smoothed over 600 data points, and independent of daily cycles, is characterized by little variability with values ranging between 0.20 and 0.26 mmol/mol (Figure 3b). Daily growth rates determined by *Daydacna* show moderate variability and are in the range of 18–27  $\mu\text{m}/\text{day}$  (Figure 3c). No manual correction, to exclude maxima not representing daily cycles, was necessary in this region of the shell. The *Daydacna* script determined  $148.2 \pm 0.08$  days (2 SD) for this measurement (Figure 3d). The precision is relatively high in this example because the result is generated in a fully automated manner, and no additional variability is introduced by manual selection. The discrepancy between the 148 days determined by the script and the optically counted 145 days is 2%. This offset between the number of days counted and determined by the script appears to be caused by a slight underestimation of the growth rate in the rim areas of the scalogram (Figure 3c).

### 3.3.2. Track 2: Variable Growth and Optically Countable Daily Bands

In the case of the second example, 271 daily bands were optically counted (Figure 4a). The density of daily bands seen in the microscope image is variable as the LA track crosses two presumably seasonal low growth areas. Mg/Ca values range from 0.10 to 0.62 mmol/mol with a mean of 0.29 mmol/mol (Figure 4b). The smoothed Mg/Ca values (600 points, LOWESS) vary between 0.21 and 0.39 mmol/mol. Two peaks in the Mg/Ca trend around 1,400 and 3,150  $\mu\text{m}$  coincide with areas of denser daily banding (Figure 4a). The detected wavelengths of daily cycles in the scalogram (Figure 4c) are variable and range between 9 and 27  $\mu\text{m}$ . In the regions of Mg/Ca peaks, daily bands were overlain by longer term frequencies. Here, *Daydacna* detected and selected wavelength

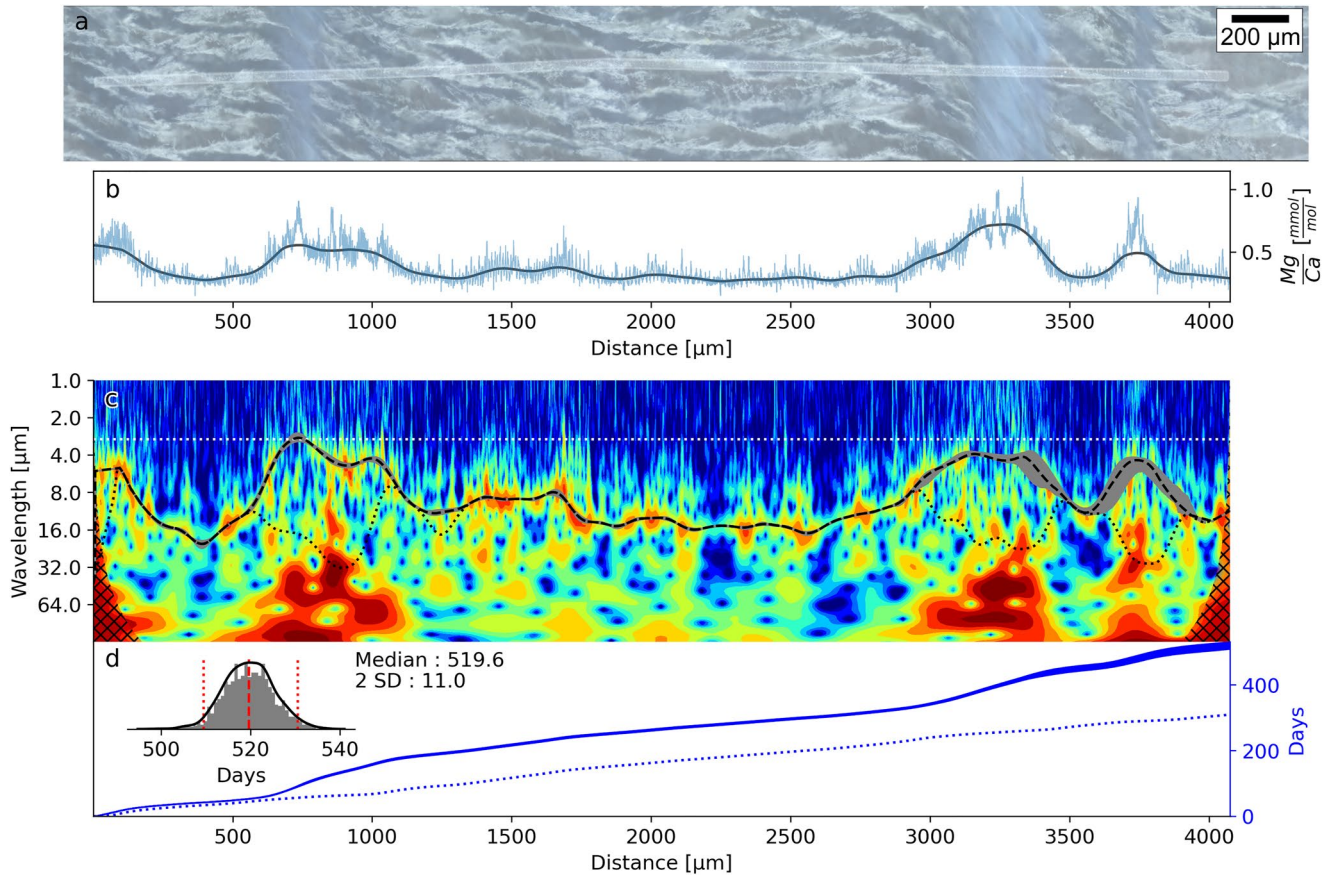


**Figure 5.** (a) Microscope image along LA track 3. Daily bands are not optically resolvable. Four dark presumably seasonal bands are visible, one of which is located at the left edge of the image. (b) Measured Mg/Ca (light blue) from LA track 3 versus distance, with daily cycles at times resolvable at the overview scale. The 600-point smoothed locally weighted scatterplot smoothing curve (gray) shows a variable long-term Mg/Ca trend with maxima around the dark bands seen in Figure 4a. (c) The determined growth rates with manual correction (dashed line) and without manual correction (dotted line) on the continuous wavelet transform scalogram of the detrended Mg/Ca are variable. The 2.5th/97.5th percentiles ( $\sim 2$  SD) area around the corrected pathway is shaded in gray. (d) The changes in the slope of the internal age model (solid blue curve) reflect the variability of growth over time, while the thickness of the blue curve reflects the 2.5th to 97.5th percentile interval, also displayed by red dotted lines in the inserted distribution graph. From the Mg/Ca signal, we determined that LA track 3 spans  $519.6 \pm 11.0$  days (2 SD). The uncorrected age model is shown in the blue dotted line.

maxima which are not related to daily bands. Hence, a manual correction was needed (Figure 4c) in order to force *Daydacna* to select the minor peaks reflecting the daily cyclicity. The manual correction is based on the optically observed shortening of daily band intervals in the regions of the dark presumably seasonal bands. The variability in growth rate can be seen in the age model displayed in time over distance (Figure 4d). The time represented in the measured shell section, as determined by *Daydacna*, is  $269.4 \pm 3.2$  days (2 SD). The 271 days counted optically are within the 2 SD interval of prediction with an offset of 2 days (0.7%).

### 3.3.3. Track 3: Variable Growth and Optically Not Countable Daily Bands

Daily bands were only partially optically visible along the third LA track, preventing continuous counting. The LA track starts within a dark presumably seasonal band and passes through another three such bands (Figure 5a). Mg/Ca values vary from 0.15 to 1.10 mmol/mol with a mean of 0.39 and the smoothed (600-point LOWESS) Mg/Ca trend ranges between 0.27 and 0.72 mmol/mol (Figure 5b). Elevated Mg/Ca values are visible in and around the dark bands (Figures 5a and 5b). The wavelengths determined by *Daydacna* range from 2 to 19  $\mu\text{m}$  (Figure 5c). Manual adjustments within the areas of the dark bands were needed for *Daydacna* to select the minor correlation peaks at higher frequencies. While better correlated higher wavelengths are present at these points in the shell, by comparison to other shell sections in which daily bands were clearly countable and based on the observation that dark bands are connected to low growth areas, we judge that the shorter wavelengths are more likely to represent daily cycles. In areas in which daily frequencies are not well represented (e.g., around 3,300  $\mu\text{m}$ , middle

of the third dark band), interpolation determines the most parsimonious pathway. The resulting growth rate is variable and decreased in the dark band areas. The determined time contained in the measured shell section is  $519.6 \pm 11.0$  days (2 SD).

### 3.4. Geochemical Composition Versus Time at Daily Resolution

The internal age models determined by *Daydacna* allow us to display the measured  $\text{El}/\text{Ca}$  data against time (Figure 6). The first LA track is ontogenetically the youngest, followed by the second and third tracks. Given that these tracks have a very similar overall length ( $\sim 4,030 \mu\text{m}$ ), the decrease in observed duration of  $\sim 150$ ,  $\sim 270$ , and  $\sim 520$  days indicates a trend towards reduced growth with increasing ontogenetic age as previously observed in our microscope image analysis. Additionally, the presence and absence of dark bands characterized by reduced growth affects the conversion of distance into time along the maximum growth axis of the shell, which *Daydacna* can account for.

Displaying the data of track 1 against time (Figure 6a; close-up in Figure 6b), using the age model derived above (Figure 3), results in clearly visible daily cycles in the  $\text{Mg}/\text{Ca}$  and  $\text{Sr}/\text{Ca}$  data sets.  $\text{Na}/\text{Ca}$  and  $\text{B}/\text{Ca}$  co-vary and display clear cycles with longer wavelengths of 4–10 days that overlie the daily cycles.  $\text{Mg}/\text{Ca}$  and  $\text{Ba}/\text{Ca}$  are characterized by low-amplitude long-term cyclic variability, while  $\text{Sr}/\text{Ca}$  shows no cyclicality other than on a daily scale.

In track 2, daily cycles are difficult to resolve in the overview image (Figure 6c). The close-up from 20 to 40 days (Figure 6d) shows distinctive daily cycles in  $\text{Mg}/\text{Ca}$  and  $\text{Sr}/\text{Ca}$ . From the overview image, we can deduce that phases of low growth, connected with high  $\text{Mg}/\text{Ca}$  values, last 1–2 months.  $\text{Mg}/\text{Ca}$  cyclicality covaries positively with  $\text{Sr}/\text{Ca}$ , whereas it displays a broadly negative relationship to  $\text{Na}/\text{Ca}$ .  $\text{B}/\text{Ca}$  behaves in an overall similar manner to  $\text{Na}/\text{Ca}$ .  $\text{Ba}/\text{Ca}$  variability increases in low growth bands.

In track 3 (Figure 6e), we observe that low-growth high  $\text{Mg}/\text{Ca}$  bands appear in the same half of the first and second years. In the other half of the first year, low  $\text{Mg}/\text{Ca}$  values prevail.  $\text{Mg}/\text{Ca}$  and  $\text{Na}/\text{Ca}$  show opposing trends in terms of their long-term variability, especially during low-growth, high  $\text{Mg}/\text{Ca}$  phases.  $\text{B}/\text{Ca}$  behaves similarly to  $\text{Na}/\text{Ca}$  in regular growth areas, but unlike  $\text{Na}/\text{Ca}$ ,  $\text{B}/\text{Ca}$  shows no strong shifts in low growth areas. The  $\text{Sr}/\text{Ca}$  variability is in phase with  $\text{Mg}/\text{Ca}$ .  $\text{Ba}/\text{Ca}$  shows an increase again in variability in low-growth areas and is lowest in the first low growth band of the second year. In the close-up view from 200 to 220 days (Figure 6f), all elemental ratios display daily cyclicality, of which  $\text{Mg}/\text{Ca}$  and  $\text{Sr}/\text{Ca}$  are clearest.

## 4. Discussion

### 4.1. LA-ICPMS Data Evaluation With *Daydacna*

*Daydacna* is a new, purposely designed Python script which allows daily resolved internal age models for (fossil) *Tridacna* shells to be generated from appropriately spatially resolved  $\text{El}/\text{Ca}$  data. Although it was only applied here on one *Tridacna* specimen, it could also be used for similar data sets generated for different biogenic or inorganic archives with incremental growth bands. Using the age model, the necessary high-resolution analysis of the geochemical parameters against time rather than shell distance is possible. We envisage that this approach could have multiple applications, such as quantified comparison between growth rate and elemental ratios, unambiguous interpretation of geochemical data in terms of seasonal paleoenvironmental change, and possible identification and quantification of extreme weather events (see Section 4.4).

Despite the excellent preservation of the inner shell part of our sample “TOBI,” where neither microscope imaging, phase (polymorph) analysis nor elemental ratios point towards recrystallization or alteration (see Section 3.1), daily increments could not be optically resolved in all parts of the inner shell. Instead, we observed that the daily geochemical variability in fossil *Tridacna* can be retrieved even in areas where daily band visibility is very poor (Figure 5, Figure S1 in Supporting Information S1). Optical evaluation of daily increments is practical within certain smaller segments with good visibility, whereas using geochemical cycles to determine daily resolved age models is advantageous for analyzing large shells with hundreds to thousands of days of growth, including shell parts with poor optical visibility. Furthermore, creating daily resolved internal age models for long-lived (several decades old) organisms using daily band counting would be very time consuming. Programs for automated image-based lamina detection have been available for over a decade (e.g., Meyer et al., 2006) and can

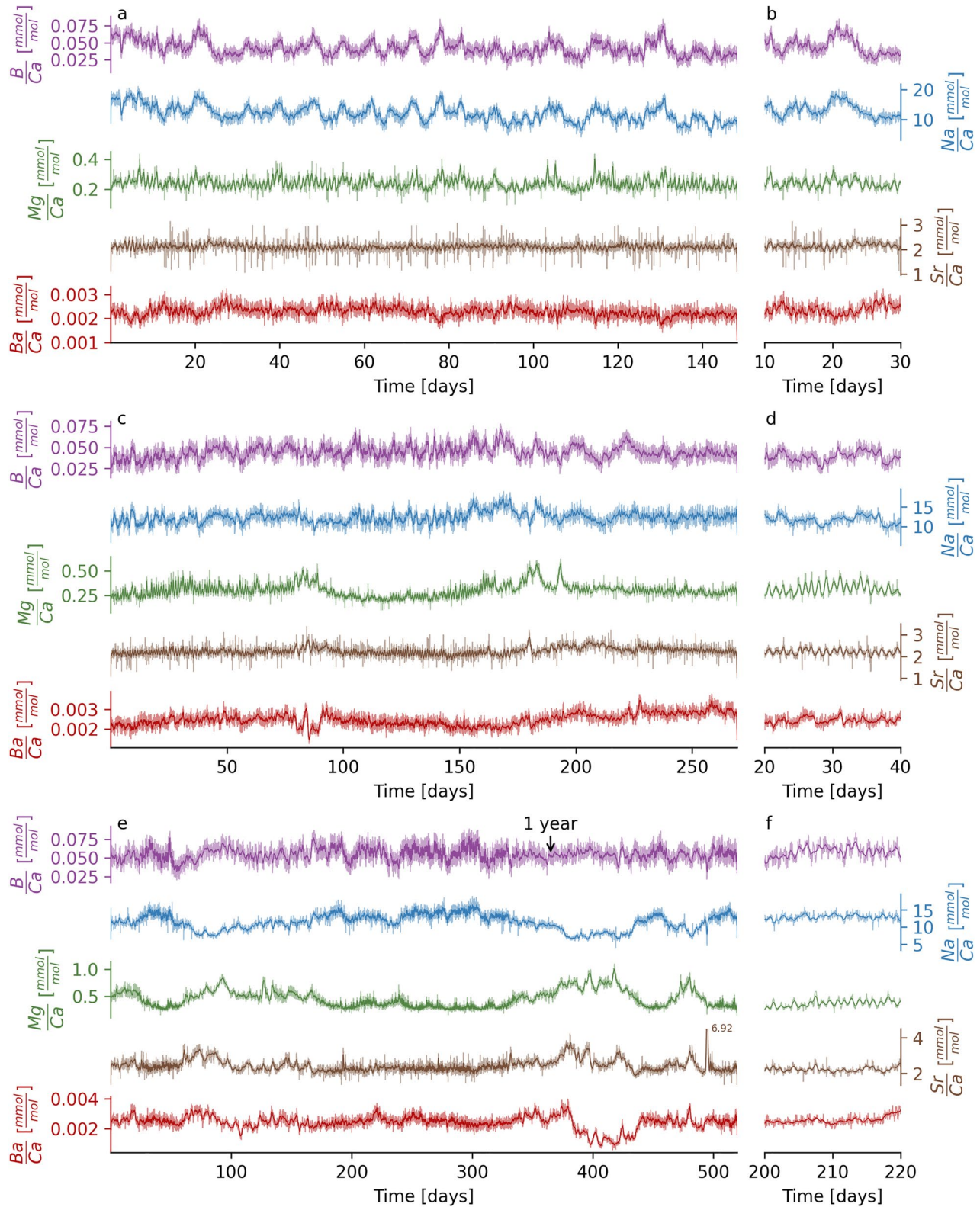


**Figure 6.** Elemental ratios for the three LA tracks (shown in Figures 3–5), now displayed versus time. The ranges of the x and y axes are specific to each track in order to best display the measured data. (a) Elemental ratios measured along LA track 1. Daily cyclicity is best visible in Mg/Ca and Sr/Ca. Overlying lower frequencies are visible in B/Ca and Na/Ca, with corresponding close-up in (b). (c) Elemental ratios measured along LA track 2 over reduced growth areas (around 80–90, and 170–200 days, respectively); (d) Close-up of c showing daily cycles for 20–40 days. (e) Elemental ratios measured along LA track 3 with four reduced growth domains (around 0–20, 70–90, 370–430, and 480–500 days), with corresponding close-up (f) for 200–220 days.

facilitate daily band counting on the scale of years if the band visibility is sufficient. However, even in areas with good banding visibility, the success of computer-based image assessment of daily bands is lower than that of geochemical assessment (Warter & Müller, 2017).

Daily geochemical cycles have previously been used in rudist shells to obtain a reliable daily resolved age model due to their better resolvability than daily banding (de Winter et al., 2020). We have extended this approach and provide, to our knowledge, the first internal age model in clams based on CWT of daily geochemical cycles. We provide a semi-automated script (*Daydacna*) which quantifies the wavelengths of the correspondent daily geochemical cycles. As the wavelength of each daily cycle indicates how much the shell grew during that day, changes in the daily wavelength over time directly translate to daily growth rates. This approach tackles both the issue of low visibility of daily banding and the time effort of counting daily signals and measuring daily signal distances over timespans of months to decades. Furthermore, one set of elemental ratio measurements can provide an age model that is directly applicable to related geochemical proxies, allowing paleoenvironmental interpretations.

#### 4.2. Before Applying *Daydacna*

To derive reasonable daily growth rates, some knowledge of the analyzed sample is needed. We interpret and restrict the selection of wavelengths, which represent daily cycles, based on the following observations, which need to be reconsidered for each sample before *Daydacna* is applied. All adaptations can be modified in the code if the underlying observations are not applicable to the specific sample under consideration; however, if the *Daydacna* code is run without adaptation, the following assumptions have to be met to obtain reliable results.

1. One band is one daily cycle:

It has previously been shown that *Tridacna* shells contain daily banding and daily cycles in Sr/Ca and Mg/Ca, likely linked to the light-related dependency of the incorporation of these elements in the shell, which could be connected to photosymbiotic activity (Sano et al., 2012; Warter & Müller, 2017; Warter et al., 2018) and/or light enhanced calcification (Rossbach et al., 2019; Sano et al., 2012). In previous *Tridacna* culturing studies, Warter et al. (2018) demonstrated that the culturing period in days was equivalent to the number of bands and cycles in several El/Ca ratios. The sample presented here (“TOBI”) is a fossil specimen, therefore we cannot independently verify how much time is contained in the shell. We observed that the Mg/Ca cycles, measured via LA-ICPMS, coincide with a microscopically detected banding pattern, similar to that observed daily in scale by Warter et al. (2018). Overall, we are confident that the El/Ca cycles in the range of a few to tens of  $\mu\text{m}$  observed in our fossil *Tridacna* are daily. The evaluation of the temporal interval of the analyzed cycles is crucial for successfully applying *Daydacna*. Other bivalves, for example, mussels, have shown semi-diurnal elemental cycles caused by semi-diurnal tidal influence (e.g., Sano et al., 2021). To analyze such samples using *Daydacna*, the expected time interval per cycle would need to be adapted.

2. Choice of appropriate widths of daily growth:

The range of daily band width observed optically within the analyzed clam fell between 2 and 38  $\mu\text{m}$ . Bands over 30  $\mu\text{m}$  wide are mostly apparent in the ontogenetic youngest part of the shell. After the first decade of life, daily growth bands in TOBI are mostly in the range of 5–25  $\mu\text{m}$ . We decided to limit the range in which correlation maxima are selected to wavelengths below 40  $\mu\text{m}$  to include all daily signals but reject long-term trends, such as seasonal signals. Shell growth rates are variable even within *Tridacnids* (from a few  $\mu\text{m}/\text{day}$  (this study) to 140  $\mu\text{m}/\text{day}$  (Killam et al., 2021)) and can range higher for other bivalves like *Pecten maximus* (e.g., Gillikin et al., 2008) or remain in the range of few  $\mu\text{m}/\text{day}$  for other calcifiers with daily banding like foraminifera (Spero et al., 2015). Therefore, it is crucial to study the sample and choose an appropriate range for daily band selection.

3. Areas displaying macroscopically dark bands coincide with reduced daily band width:

We observed a linkage between the macroscopically dark (translucent) bands and low growth rate (see Section 3.2). The signal of daily cycles in the low growth rate range, close to or below the spot size (i.e., slit width; 3  $\mu\text{m}$ ), can be reduced in amplitude due to smoothing effects. Sinusoidal signals with wavelengths of the spot size/ $n$ , with  $n \in \mathbb{N}$ , cannot be detected. In these areas of reduced daily cycle amplitudes, the daily signal is often overlain by cyclicities with larger wavelengths. The overlying signal is not reduced in amplitude and may dominate during the evaluation of correlation maxima in the scalogram, making it more likely to be automatically selected by the script than the daily signal. Therefore, manual corrections are often needed

in these areas of low growth rate, implying that in such cases the shorter wavelengths should preferably be selected manually.

4. Shifts in growth rate are gradual:

Based on microscope images, shifts in daily band widths are gradual rather than abrupt such that slight differences in width between individual daily bands can be averaged out without biasing the age model overall. As such, smoothed correlation curves of the scalogram are used to select the correlation maxima most likely related to daily cycles and the growth rate pathways are smoothed again to exclude unrealistically abrupt short-term variability in the suggested growth rate.

### 4.3. *Daydacna* Limitations

A prerequisite for the effective use of our *Daydacna* script for internal age assessment is the availability of appropriate data sets on shell structure (imaging) and geochemical composition (Section 4.2). The major limitation of the script is that not all auto-selected correlation maxima are necessarily related to daily cycles, which necessitates some manual adjustment. In the case of the specimen studied here, we observed that the daily cycle signal is usually well visible in the scalogram. The lower limit of cyclic signal detection is twice the sampling frequency (e.g., Åström, 1969), allowing the detection of cycles with wavelengths down to 0.7  $\mu\text{m}$  in our data. But due to smoothing effects caused by the fact that the spot size (3  $\mu\text{m}$ ) is larger than the sampling steps ( $\sim 0.35 \mu\text{m}$ ), we cannot detect sinusoidal signals with wavelengths of the spot size/ $n$  with  $n \in \mathbb{N}$  (i.e., 3, 1.5, 1, and 0.75  $\mu\text{m}$ ). Cyclic signal detection below the spot size is both severely reduced in amplitude and discontinuous and thus less reliable. We recommend using a spot size below the smallest expected wavelengths to analyze the cyclic signal. For our specimen, optically determined daily banding as well as detected daily cycle wavelengths are rarely below the spot size. However, cyclic signals with wavelengths above the spot size also have a smoothing-induced reduction in amplitude, which is more pronounced the closer the wavelength is to the spot size. The resulting biases in the automatic selection of correlation maxima toward longer wavelengths can affect the resulting internal age model. This underlines the importance of the manual adjustment option, which allows manually selected points to replace those automatically selected in the first step. A range of interest is set via Monte Carlo simulation in the case of both manual and automatic selection, in which *Daydacna* automatically searches for maxima a second time. An exact selection of the minor correlation peaks associated with daily cycle wavelengths is not needed as the position of the point is subsequently varied via Monte Carlo simulation, such that similar pathway corrections lead to equivalent results with deviations of no more than a few percentage. However, it is possible to manually select areas which do not represent daily cycles, which can lead to erroneous growth rates. The resulting growth model should therefore be checked in a few test cases before applying it to larger data sets.

To assess whether the resultant model is realistic, two approaches can be taken. In areas with countable daily growth bands, a comparison between the number of daily growth bands and the number of days suggested by the age model can be conducted to check the accuracy of the model (see results; Figures 3 and 4). This is especially suitable for testing the model on shorter intervals within the shell before selecting larger shell segments. In areas without countable daily bands and across longer areas of the shell, the evenness of daily cycles over time can be checked via wavelet transformation of the geochemical data onto their timescale. However, note that the wavelet transformation can only be applied to evenly spaced data. As the measured data are redistributed from distance to time by *Daydacna*, the resulting data points will be unevenly distributed. Therefore, resampling of the data along the interpolated pathways between the measured data points must be conducted beforehand. After rescaling the geochemical signal over time, daily cycles should be uniform and, by definition, 1 day long. In the resulting wavelet scalogram of the detrended data set, we expect the highest correlation around the one-day wavelength if the manual selection of the daily wavelength area is accurate (Figure S12 in Supporting Information S1). If there are areas where the correlation maxima strongly deviate from the 1-day line, the time contained in this interval may have been over- or underestimated. In this case, the section of data should be reconsidered by adapting the manual selection of the pathway such that the resulting scalogram of the daily cycles shows frequencies in the 1-day range.

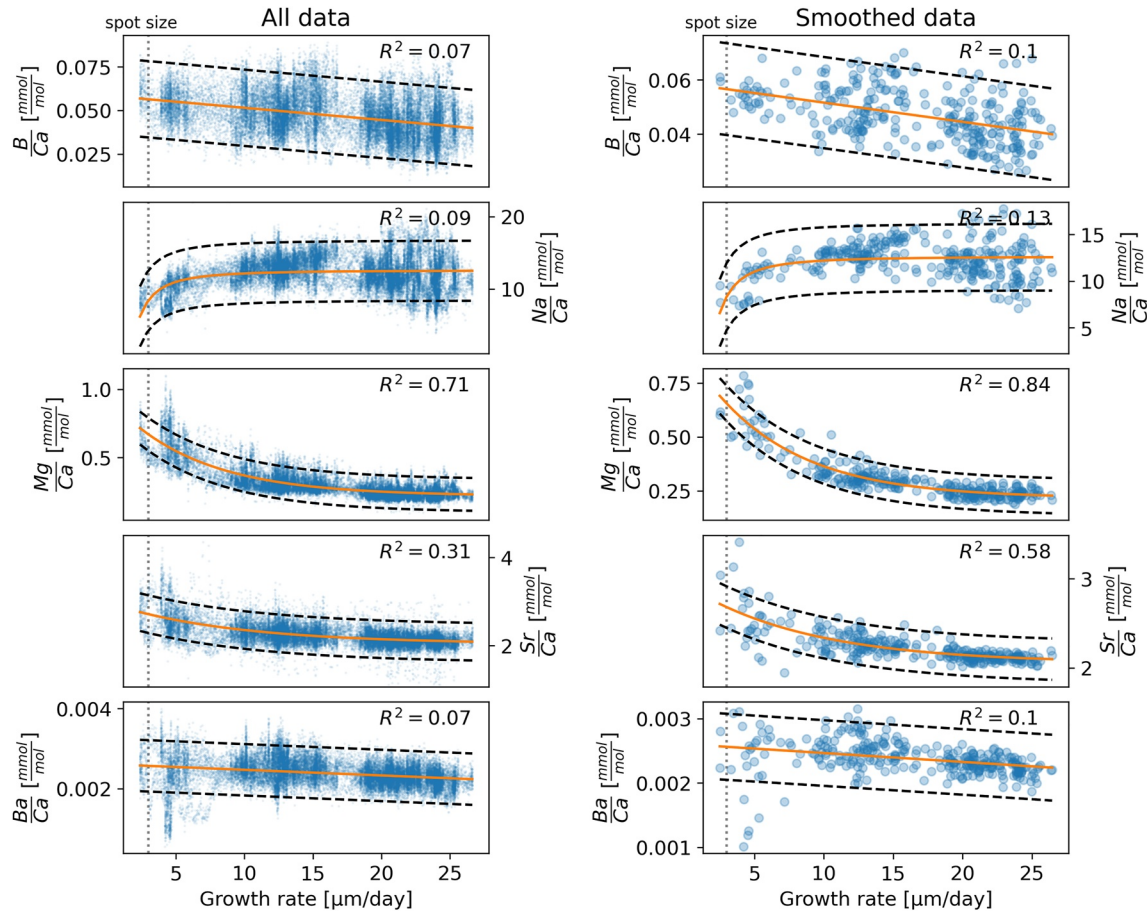


**Figure 7.** Correlation curves of growth rate versus EI/Ca ratios of all three LA tracks. All data ( $n = 35,061$ ) are displayed on the left in semi-transparent blue dots to better show the data density, while the data smoothed over 120 points ( $n = 294$ ) are displayed on the right in semi-transparent circles. Dashed lines represent the upper and lower 95% prediction band (95% chance that the next data point is within that area). The 95% confidence interval lies almost indistinguishably close to the regression line (orange) due to the large data set and is therefore not displayed.

#### 4.4. Dayacna Applications

##### 4.4.1. EI/Ca Variability With Growth Rate

Macroscopically visible darker seasonal bands and thus areas with low growth rates coincide with higher Mg/Ca, as has previously been shown in other mollusks (e.g., Lorenz & Bender, 1977; Schliekofer et al., 2021). Here, we demonstrate one advantage of deriving a continuous growth rate model by testing whether Mg/Ca and other elemental ratios correlate with the growth rates determined (Figure 7). Mg/Ca values and growth rate correlate nonlinearly and negatively with an  $R^2$  value of 0.71, increasing to 0.84 in the case of the corresponding smoothed data set that excludes daily variability. Similarly, Sr/Ca shows a nonlinear and negative trend with an  $R^2$  value of 0.31 for the complete data set and 0.58 for the smoothed data set. Na/Ca shows a nonlinear but positive trend with a growth rate mostly in the low growth areas, with overall poor correlation coefficients. Both B/Ca and Ba/Ca show an essentially linear increase with lower growth rates albeit with a shallow slope and lower coefficient of correlation ( $R^2$  value of 0.07 for both ratios for the untreated data and 0.1 for the smoothed data). By correlating Ba/Ca to growth rate, we could, however, confirm our previous observation (Figures 6c and 6e) that Ba/Ca variability increases in low growth areas. Similarly, the Mg/Ca and Sr/Ca variability is higher for low growth rates.

##### 4.4.2. Seasonal Environmental Impacts

Evaluating seasonal paleoenvironmental data on daily resolved time scales rather than over distance improves data comparability over several years and between different organisms and time periods. In the following section, we briefly discuss the sub-seasonally-resolved paleoenvironmental information that can be gleaned from different

elemental ratios. Overall, an investigation across greater time spans would be needed for an in depth paleoenvironmental interpretation, as reproducible seasonal patterns would become more evident. However, the observations, especially from track 3, already point towards a long-term trend in shell geochemistry with seasonal variability. The low growth bands, visible as dark bands in the shell, occur typically twice a year and are associated with long-term changes in Mg/Ca, Sr/Ca, Ba/Ca, and Na/Ca. Mg/Ca and to a lesser extent Sr/Ca values are increased in low growth areas (Figure 7), whereas Na/Ca decreases in these bands. The measured Ba/Ca is characterized by a higher degree of variability in seasonal intervals of low growth.

**Mg/Ca** displays a strong relationship with growth rate (Section 4.4.1, Figure 7). Previous studies link Mg/Ca ratios in *Tridacna* to temperature (Arias-Ruiz et al., 2017; Ayling et al., 2015; Warter et al., 2015) as well as light availability and physiological stress, especially on short (daily) time scales (Warter et al., 2018). In *Arctica islandica* shells, a correlation between increased Mg and increased organics (in the form of the organic matrix) has been observed (Schöne et al., 2010) as well as a dependency on the crystal structure (Schöne et al., 2013). In *Tridacna*, Mg/Ca has also been suggested to be growth-dependent given the increasing Mg/Ca with ontogenetic age (e.g., Elliot et al., 2009; Warter et al., 2015). We propose that the growth rate also impacts Mg/Ca at much shorter time scales, from daily to seasonal. On the daily level, the Mg/Ca ratios provide the clearest of the El/Ca cycles. This might be due to the impact of reduced growth during the night, characterized by elevated Mg/Ca values, and vice versa (cf., Warter et al., 2018). In bivalves, reduced growth and elevated Mg/Ca values can also be coupled to a relative increase in organic content (Schleinkofer et al., 2021).

More broadly, these findings suggest that it is unlikely that a single environmental parameter governs shell Mg/Ca. Instead, both temperature and light are impacting the growth rate, crystal structure, and possibly incorporation of organics into the organism shell and thus affect Mg/Ca values. Decoupling the effect of temperature, light, and growth rate in experimental setups would greatly aid the development of the proxy. However, given that Mg/Ca is dominantly driven by growth rate (or some factor that correlates with growth rate), irrespective of the primary cause of the change in growth rate, the Mg/Ca “proxy” may find utility as a tracer of the combined set of processes that can impact the calcification rate. We expect that during the rainy season, irradiance is reduced because of reduced direct sunlight and higher turbidity. This causes reduced growth and high Mg/Ca values. Mg/Ca may thus be used to track growth rate changes, possibly linked to seasonal rainfall. Hence, the recording of the rainy season, coupled to the passing of the Intertropical Convergence Zone (ITCZ) twice a year, may make Mg/Ca in *Tridacna* a potential tracer for past ITCZ positioning in tropical regions.

**Sr/Ca** values show a slight increase in low growth areas, but no strong correlation between growth rate and Sr/Ca could be established. Contradicting observations have been documented regarding the interpretation of Sr/Ca as a paleoenvironmental proxy in *Tridacna*. While some studies show a partly species-dependent, inverse correlation between Sr/Ca and SST (Mei et al., 2018; Yan et al., 2013), other studies found no significant correlation (Arias-Ruiz et al., 2017; Batenburg et al., 2011; Elliot et al., 2009; Warter et al., 2015). On a smaller scale, the diurnal Sr/Ca cycles have been linked to diurnal changes in irradiance (Hori et al., 2015; Sano et al., 2012). Sr/Ca variability has also been linked to physiological performance and growth (Carré et al., 2006; Gillikin et al., 2005). In our data, long-term Sr/Ca trends are in phase with Mg/Ca but the correlation to growth rate is weaker in the former (Figure 7). A dependency of Sr/Ca on solar irradiance could explain the high Sr/Ca values associated with the dark seasonal banding, which we interpret as growth during the rainy season in which the reef experiences reduced direct sunlight and increased water turbidity.

**Ba/Ca** in *Tridacna* has been proposed as an indicator of primary productivity (Arias-Ruiz et al., 2017; Elliot et al., 2009; Hori et al., 2015) and other mollusks (e.g., Fröhlich et al., 2022; Gillikin et al., 2008; Marali et al., 2017). Short and intense Ba/Ca peaks have also been connected to storm events in *Tridacna* (Komagoe et al., 2018) and Tsunamis in mussels (Sano et al., 2021). A higher variability during low growth (Figure 7) might indicate an increased storm activity during the rainy season, additionally impacting turbidity and nutrient availability through influx and resuspension and thus introducing higher variability in primary productivity.

**Na/Ca** is yet to be established as a paleoenvironmental proxy in *Tridacna*. Na/Ca has been positively correlated with salinity (negatively to freshening) in marine mollusks (Findlater et al., 2014) and estuarine barnacles (Gordon et al., 1970). Similarly, Na/Ca was suggested to be a proxy for salinity in foraminifera (Wit et al., 2013). However, the very weak relationship of Na/Ca to salinity in core-top samples and similarly weak relationships to other environmental factors, such as temperature, seawater  $[\text{CO}_3^{2-}]$ , and bottom water  $\Omega_{\text{calcite}}$ , make its successful application as a salinity proxy unlikely in most settings (Gray et al., 2023). If the Na/Ca-salinity relationship in



mollusks is indeed expressed more strongly than in foraminifera, the Na/Ca decrease observed in periods with low growth rates could be related to a freshening happening in the rainy season. However, more experimental data are needed to robustly interpret this elemental ratio.

## 5. Conclusions and Outlook

We present our Python script *Daydacna*, which enables an age model to be created, using CWT analysis of elemental data of samples with daily resolution chemical banding, applied here to a fossil *Tridacna* shell. A key advantage of this approach is that the spatially resolved measured data are assigned to regular time intervals using an age model based on the data itself. This approach avoids potential errors introduced by matching the geochemical data set to the optical data set and reduces the dependence on the optical resolvability of daily banding, making it both more time efficient and applicable to more samples compared to optical approaches. By applying the age, seasonal changes in environmental proxy data over time can be assessed at the daily temporal resolution. Furthermore, the daily growth rates are quantified across the shell and can be compared to elemental ratios. We show that Mg/Ca is growth rate dependent and suggest considering the influence of metabolism and growth rate driven incorporation of organic matter and trace elements in addition to the influence of external environmental factors (e.g., temperature or light) impacting the element incorporation into the shell. Further in-depth evaluation of growth rate changes, how they are impacted by environmental changes and how they affect elemental incorporation is needed, based on culturing studies with controlled environmental settings (cf., Warter et al., 2018).

The *Daydacna* script with its CWT approach to reconstruct daily cycles provides a basis for further paleoseasonality and growth rate studies in *Tridacna* (and potentially other long-lived mollusks with daily chemical growth bands). Ultimately, we envisage that this approach of combining daily resolved geochemical data with a daily growth model will facilitate the interpretation of geochemical data sets from clams in terms of paleo(extreme) weather evaluation, given that several El/Ca systems have been shown to relate closely to light intensity and/or chemical and physical properties of the seawater (e.g., Arias-Ruiz et al., 2017; Ayling et al., 2015; Hori et al., 2015; Sano et al., 2012; Warter et al., 2015, 2018). *Tridacna* shells can provide decade-long records of the tropics and subtropics from the early Miocene onwards (Harzhauser et al., 2008). They are therefore especially well-suited for the generation of decade-long paleo(extreme)weather and seasonality records in the context of Neogene (sub)tropical climate reconstructions.

Although *Daydacna* was designed to evaluate daily cycles in *Tridacna* samples, it can be applied to other archives, types of data sets, or cyclicities. Potential high-resolution archives suitable for *Daydacna* include other bivalves, corals, coralline algae, otoliths, other marine calcifiers, speleothems and teeth. If geochemical data are not retrievable in sub-daily resolution, other types of cyclic data sets can be used to evaluate daily cycles with *Daydacna*, such as a lightness or color curve across a sample which shows distinct daily banding throughout the shell. If the lowest measurable cyclicity in the data set is tidal, yearly, or even in the scale of Milankovitch cycles, the script could still be applied by adjusting the defined length for one cycle, as long as the time represented by one cycle is well known. Lastly, if low frequency cycles of known time spans are available within the sample (e.g., yearly cycles), *Daydacna* can also be used to assess which time interval fits best to the high frequency cycles of the same data set (e.g., diurnal or semi-diurnal).

## Data Availability Statement

The laser-ablation data fed into *Daydacna* to create the internal age models in this study are available at Zenodo with licence CC BY 4.0 (Arndt et al., 2023). Version 1 of *Daydacna* used to create an internal age model and redistribute data from distance to time is available at Zenodo with licence CC BY 4.0 (Arndt & Coenen, 2023).

## References

- Aharon, P. (1991). Recorders of reef environment histories: Stable isotopes in corals, giant clams, and calcareous algae. *Coral Reefs*, 10(2), 71–90. <https://doi.org/10.1007/BF00571826>
- Arias-Ruiz, C., Elliot, M., Bézoz, A., Pedoja, K., Husson, L., Cahyarini, S. Y., et al. (2017). Geochemical fingerprints of climate variation and the extreme La Niña 2010–11 as recorded in a *Tridacna squamosa* shell from Sulawesi, Indonesia. *Palaeogeography, Palaeoclimatology, Palaeoecology*, 487, 216–228. <https://doi.org/10.1016/j.palaeo.2017.08.037>
- Arndt, I., & Coenen, D. (2023). *Daydacna* [Code]. Zenodo. <https://doi.org/10.5281/zenodo.8334594>

### Acknowledgments

We are grateful for a scholarship of the Stiftung Polytechnische Gesellschaft that provided financial support for the corresponding author as well as funding via the Deutsche Forschungsgemeinschaft grant (DFG MU 3739/6-1). We thank Linda Marko, Alexander Schmidt, and Richard Albert for technical support during LA-ICPMS measurements, data reduction and microscope imaging. Maria Bladt, Sören Tholen, and Niels Parawitz are thanked for the preparation of the sample slabs and thin sections. Our gratitude also goes to Renate Rabenstein for X-ray and  $\mu$ CT imaging and Wolfgang Schiller for fluorescence microscope imaging. We thank Rainer Petschick and Ruben Rittberger for assisting with the visualization of the XRD and ATR-FTIR data, respectively. We gratefully acknowledge discussions with Viola Warter and Max Fursman. Aspects of this research (DC, DE, WM) were co-funded through the VeWA consortium (Past Warm Periods as Natural Analogues of our high-CO<sub>2</sub> Climate Future) by the LOEWE programme of the Hessen Ministry of Higher Education, Research and the Arts, Germany. FIERCE is financially supported by the Wilhelm and Else Heraeus Foundation and by the Deutsche Forschungsgemeinschaft (DFG: INST 161/921-1 FUGG, INST 161/923-1 FUGG and INST 161/1073-1 FUGG), which is gratefully acknowledged. This is FIERCE contribution No. 140. Open Access funding enabled and organized by Projekt DEAL.

- Arndt, I., Coenen, D., Evans, D., Renema, W., & Müller, W. (2023). Supplementary Data to 'Quantifying sub-seasonal growth rate changes in fossil giant clams using wavelet transformation of daily Mg/Ca cycles' in Geochemistry, Geophysics, Geosystems [Dataset]. Zenodo. <https://doi.org/10.5281/zenodo.7755711>
- Åström, K. J. (1969). On the choice of sampling rates in parametric identification of time series. *Information Sciences*, *1*(3), 273–278. [https://doi.org/10.1016/S0020-0255\(69\)80013-7](https://doi.org/10.1016/S0020-0255(69)80013-7)
- Ayling, B. F., Chappell, J., Gagan, M. K., & McCulloch, M. T. (2015). ENSO variability during MIS 11 (424–374 ka) from *Tridacna gigas* at Huon Peninsula, Papua New Guinea. *Earth and Planetary Science Letters*, *431*, 236–246. <https://doi.org/10.1016/j.epsl.2015.09.037>
- Batenburg, S. J., Reichart, G.-J., Jilbert, T., Janse, M., Wesselingh, F. P., & Renema, W. (2011). Interannual climate variability in the Miocene: High resolution trace element and stable isotope ratios in giant clams. *Palaeogeography, Palaeoclimatology, Palaeoecology*, *306*(1–2), 75–81. <https://doi.org/10.1016/j.palaeo.2011.03.031>
- Carré, M., Bentaleb, I., Bruguier, O., Ordino, E., Barrett, N. T., & Fontugne, M. (2006). Calcification rate influence on trace element concentrations in aragonitic bivalve shells: Evidences and mechanisms. *Geochimica et Cosmochimica Acta*, *70*(19), 4906–4920. <https://doi.org/10.1016/j.gca.2006.07.019>
- Carré, M., & Cheddadi, R. (2017). Seasonality in long-term climate change. *Quaternaire. Revue de l'Association Française Pour l'étude Du Quaternaire*, *28*(2), 173–177. <https://doi.org/10.4000/quaternaire.8018>
- Caswell, T. A., Droettboom, M., Lee, A., de Andrade, E. S., Hoffmann, T., Klymak, J., et al. (2022). matplotlib/matplotlib: REL: V3.5.2 [Software]. Zenodo. <https://doi.org/10.5281/zenodo.6513224>
- Cauquoin, A., Werner, M., & Lohmann, G. (2019). Water isotopes – Climate relationships for the mid-Holocene and preindustrial period simulated with an isotope-enabled version of MPI-ESM. *Climate of the Past*, *15*(6), 1913–1937. <https://doi.org/10.5194/cp-15-1913-2019>
- Cleveland, W. S. (1979). Robust locally weighted regression and smoothing scatterplots. *Journal of the American Statistical Association*, *74*(368), 829–836. <https://doi.org/10.2307/2286407>
- de Winter, N. J., Goderis, S., Malderen, S. J. M. V., Sinnesael, M., Vansteenberge, S., Snoeck, C., et al. (2020). Subdaily-scale chemical variability in a *Torreites Sanchezi* rudist shell: Implications for rudist paleobiology and the Cretaceous day-night cycle. *Paleoceanography and Paleoclimatology*, *35*(2), e2019PA003723. <https://doi.org/10.1029/2019PA003723>
- Driscoll, R., Elliot, M., Russon, T., Welsh, K., Yokoyama, Y., & Tudhope, A. (2014). ENSO reconstructions over the past 60 ka using giant clams (*Tridacna* sp.) from Papua New Guinea. *Geophysical Research Letters*, *41*(19), 6819–6825. <https://doi.org/10.1002/2014GL061446>
- Duprey, N., Lazareth, C. E., Dupouy, C., Butscher, J., Farman, R., Maes, C., & Cabioch, G. (2015). Calibration of seawater temperature and  $\delta^{18}\text{O}_{\text{seawater}}$  signals in *Tridacna maxima*'s  $\delta^{18}\text{O}_{\text{shell}}$  record based on in situ data. *Coral Reefs*, *34*(2), 437–450. <https://doi.org/10.1007/s00338-014-1245-z>
- Elliot, M., Welsh, K., Chilcott, C., McCulloch, M., Chappell, J., & Ayling, B. (2009). Profiles of trace elements and stable isotopes derived from giant long-lived *Tridacna gigas* bivalves: Potential applications in paleoclimate studies. *Palaeogeography, Palaeoclimatology, Palaeoecology*, *280*(1–2), 132–142. <https://doi.org/10.1016/j.palaeo.2009.06.007>
- Evans, D., & Müller, W. (2018). Automated extraction of a five-year LA-ICP-MS trace element data set of ten common glass and carbonate reference materials: Long-term data quality, optimisation and laser cell homogeneity. *Geostandards and Geoanalytical Research*, *42*(2), 159–188. <https://doi.org/10.1111/ggr.12204>
- Fietzke, J., & Frische, M. (2016). Experimental evaluation of elemental behavior during LA-ICP-MS: Influences of plasma conditions and limits of plasma robustness. *Journal of Analytical Atomic Spectrometry*, *31*(1), 234–244. <https://doi.org/10.1039/C5JA00253B>
- Findlater, G., Shelton, A., Rolin, T., & Andrews, J. (2014). Sodium and strontium in mollusc shells: Preservation, palaeosalinity and palaeotemperature of the Middle Pleistocene of eastern England. *Proceedings of the Geologists' Association*, *125*(1), 14–19. <https://doi.org/10.1016/j.pgeola.2013.10.005>
- Foster, L. C., Andersson, C., Høje, H., Allison, N., Finch, A. A., & Johansen, T. (2008). Effects of micromilling on  $\delta^{18}\text{O}$  in biogenic aragonite. *Geochemistry, Geophysics, Geosystems*, *9*(4), Q04013. <https://doi.org/10.1029/2007GC001911>
- Fröhlich, L., Siebert, V., Walliser, E. O., Thébaud, J., Jochum, K. P., Chauvaud, L., & Schöne, B. R. (2022). Ba/Ca profiles in shells of *Pecten maximus* – A proxy for specific primary producers rather than bulk phytoplankton. *Chemical Geology*, *593*, 120743. <https://doi.org/10.1016/j.chemgeo.2022.120743>
- Füllenbach, C. S., Schöne, B. R., Shirai, K., Takahata, N., Ishida, A., & Sano, Y. (2017). Minute co-variations of Sr/Ca ratios and microstructures in the aragonitic shell of *Cerastoderma edule* (Bivalvia) – Are geochemical variations at the ultra-scale masking potential environmental signals? *Geochimica et Cosmochimica Acta*, *205*, 256–271. <https://doi.org/10.1016/j.gca.2017.02.019>
- Gannon, M. E., Pérez-Huerta, A., Aharon, P., & Street, S. C. (2017). A biomineralization study of the Indo-Pacific giant clam *Tridacna gigas*. *Coral Reefs*, *36*(2), 503–517. <https://doi.org/10.1007/s00338-016-1538-5>
- Garbe-Schönberg, D., & Müller, S. (2014). Nano-particulate pressed powder tablets for LA-ICP-MS. *Journal of Analytical Atomic Spectrometry*, *29*(6), 990–1000. <https://doi.org/10.1039/C4JA00007B>
- Gillikin, D. P., Lorrain, A., Navez, J., Taylor, J. W., André, L., Keppens, E., et al. (2005). Strong biological controls on Sr/Ca ratios in aragonitic marine bivalve shells. *Geochemistry, Geophysics, Geosystems*, *6*(5), Q05009. <https://doi.org/10.1029/2004GC000874>
- Gillikin, D. P., Lorrain, A., Paulet, Y.-M., André, L., & Dehairs, F. (2008). Synchronous barium peaks in high-resolution profiles of calcite and aragonite marine bivalve shells. *Geo-Marine Letters*, *28*(5), 351–358. <https://doi.org/10.1007/s00367-008-0111-9>
- Gordon, C. M., Carr, R. A., & Larson, R. E. (1970). The influence of environmental factors on the sodium and manganese content of Barnacle shells. *Limnology & Oceanography*, *15*(3), 461–466. <https://doi.org/10.4319/lo.1970.15.3.0461>
- Goupillaud, P., Grossmann, A., & Morlet, J. (1984). Cycle-octave and related transforms in seismic signal analysis. *Geoexploration*, *23*(1), 85–102. [https://doi.org/10.1016/0016-7142\(84\)90025-5](https://doi.org/10.1016/0016-7142(84)90025-5)
- Gray, W. R., Evans, D., Henahan, M., Weldeab, S., Lea, D. W., Müller, W., & Rosenthal, Y. (2023). Sodium incorporation in foraminiferal calcite: An evaluation of the Na/Ca salinity proxy and evidence for multiple Na-bearing phases. *Geochimica et Cosmochimica Acta*, *348*, 152–164. <https://doi.org/10.1016/j.gca.2023.03.011>
- Harris, C. R., Millman, K. J., van der Walt, S. J., Gommers, R., Virtanen, P., Cournapeau, D., et al. (2020). Array programming with NumPy. *Nature*, *585*(7825), 357–362. <https://doi.org/10.1038/s41586-020-2649-2>
- Harzhauser, M., Mandic, O., Piller, W. E., Reuter, M., & Kroh, A. (2008). Tracing back the origin of the Indo-Pacific Mollusc Fauna: Basal Tridacninae from the Oligocene and Miocene of the Sultanate of Oman. *Palaeontology*, *51*(1), 199–213. <https://doi.org/10.1111/j.1475-4983.2007.00742.x>
- Hori, M., Sano, Y., Ishida, A., Takahata, N., Shirai, K., & Watanabe, T. (2015). Middle Holocene daily light cycle reconstructed from the strontium/calcium ratios of a fossil giant clam shell. *Scientific Reports*, *5*(1), 8734. <https://doi.org/10.1038/srep08734>
- Jantzen, C., Wild, C., El-Zibdah, M., Roa-Quiaoit, H. A., Haacke, C., & Richter, C. (2008). Photosynthetic performance of giant clams, *Tridacna maxima* and *T. squamosa*, Red Sea. *Marine Biology*, *155*(2), 211–221. <https://doi.org/10.1007/s00227-008-1019-7>

- Jochum, K. P., Scholz, D., Stoll, B., Weis, U., Wilson, S. A., Yang, Q., et al. (2012). Accurate trace element analysis of speleothems and biogenic calcium carbonates by LA-ICP-MS. *Chemical Geology*, 318–319, 31–44. <https://doi.org/10.1016/j.chemgeo.2012.05.009>
- Jochum, K. P., Stoll, B., Herwig, K., Willbold, M., Hofmann, A. W., Amini, M., et al. (2006). MPI-DING reference glasses for in situ microanalysis: New reference values for element concentrations and isotope ratios. *Geochemistry, Geophysics, Geosystems*, 7(2), Q02008. <https://doi.org/10.1029/2005GC001060>
- Jochum, K. P., Weis, U., Stoll, B., Kuzmin, D., Yang, Q., Raczek, I., et al. (2011). Determination of reference values for NIST SRM 610–617 glasses following ISO guidelines. *Geostandards and Geoanalytical Research*, 35(4), 397–429. <https://doi.org/10.1111/j.1751-908X.2011.00120.x>
- Killam, D., Al-Najjar, T., & Clapham, M. (2021). Giant clam growth in the Gulf of Aqaba is accelerated compared to fossil populations. *Proceedings of the Royal Society B: Biological Sciences*, 288(1957), 20210991. <https://doi.org/10.1098/rspb.2021.0991>
- Komagoe, T., Watanabe, T., Shirai, K., Yamazaki, A., & Uematu, M. (2018). Geochemical and microstructural signals in giant clam *Tridacna maxima* recorded typhoon events at Okinotori Island, Japan. *Journal of Geophysical Research: Biogeosciences*, 123(5), 1460–1474. <https://doi.org/10.1029/2017JG004082>
- Kunzmann, A. (2008). Physiological performance of giant clams (*Tridacna spec.*) in a recirculation system. In *ICRS Conference Proceedings* (pp. 316–320). Retrieved from [https://nsuworks.nova.edu/occ\\_icrs/1](https://nsuworks.nova.edu/occ_icrs/1)
- Longerich, H. P., Jackson, S. E., & Günther, D. (1996). Inter-laboratory note. Laser ablation inductively coupled plasma mass spectrometric transient signal data acquisition and analyte concentration calculation. *Journal of Analytical Atomic Spectrometry*, 11(9), 899–904. <https://doi.org/10.1039/JA9961100899>
- Lorens, R. B., & Bender, M. L. (1977). Physiological exclusion of magnesium from *Mytilus edulis* calcite. *Nature*, 269, 5631–5794. <https://doi.org/10.1038/269793a0>
- Ma, X., Yan, H., Fei, H., Liu, C., Shi, G., Huang, E., et al. (2020). A high-resolution  $\delta^{18}\text{O}$  record of modern *Tridacna gigas* bivalve and its paleoenvironmental implications. *Palaeogeography, Palaeoclimatology, Palaeoecology*, 554, 109800. <https://doi.org/10.1016/j.palaeo.2020.109800>
- Marali, S., Schöne, B. R., Mertz-Kraus, R., Griffin, S. M., Wanamaker, A. D., Matras, U., & Butler, P. G. (2017). Ba/Ca ratios in shells of *Arctica islandica* – Potential environmental proxy and crossdating tool. *Palaeogeography, Palaeoclimatology, Palaeoecology*, 465, 347–361. <https://doi.org/10.1016/j.palaeo.2015.12.018>
- Mei, Y., Shao, D., Wang, Y., Yang, Z., Yang, W. Q., Gao, Y., et al. (2018). Measurement of Sr/Ca ratio in *Tridacna spp.* Shells from South China Sea: A comparison of SR-XRF and ICP-OES analysis methods. *Spectroscopy and Spectral Analysis*, 38(5), 1640–1647. [https://doi.org/10.3964/j.issn.1000-0593\(2018\)05-1640-08](https://doi.org/10.3964/j.issn.1000-0593(2018)05-1640-08)
- Meyer, M. C., Faber, H., & Spötl, C. (2006). The WinGeol Lamination Tool: New software for rapid, semi-automated analysis of laminated climate archives. *The Holocene*, 16(5), 753–761. <https://doi.org/10.1191/0959683606hl969rr>
- Morlet, J., Arens, G., Fourgeau, E., & Glard, D. (1982). Wave propagation and sampling theory; Part I: Complex signal and scattering in multi-layered media. *Geophysics*, 47(2), 203–221. <https://doi.org/10.1190/1.1441328>
- Müller, W., Shelley, M., Miller, P., & Broude, S. (2009). Initial performance metrics of a new custom-designed ArF excimer LA-ICPMS system coupled to a two-volume laser-ablation cell. *Journal of Analytical Atomic Spectrometry*, 24(2), 209–214. <https://doi.org/10.1039/B805995K>
- Paton, C., Hellstrom, J., Paul, B., Woodhead, J., & Hergt, J. (2011). Iolite: Freeware for the visualisation and processing of mass spectrometric data. *Journal of Analytical Atomic Spectrometry*, 26(12), 2508–2518. <https://doi.org/10.1039/C1JA10172B>
- Pätzold, J., Heinrichs, J. P., Wolschendorf, K., & Wefer, G. (1991). Correlation of stable oxygen isotope temperature record with light attenuation profiles in reef-dwelling *Tridacna* shells. *Coral Reefs*, 10(2), 65–69. <https://doi.org/10.1007/BF00571825>
- Reback, J., jbrockmendel, McKinney, W., Bossche, J. V. D., Roeschke, M., Augspurger, T., et al. (2022). pandas-dev/pandas: Pandas 1.4.3 [Software]. Zenodo. <https://doi.org/10.5281/zenodo.6702671>
- Renema, W., Warter, V., Novak, V., Young, J. R., Marshall, N., & Hasibuan, F. (2015). Ages of Miocene fossil localities in the northern Kutai Basin (East Kalimantan, Indonesia). *PALAIOS*, 30(1), 26–39. <https://doi.org/10.2110/palo.2013.127>
- Rosbach, S., Saderne, V., Anton, A., & Duarte, C. M. (2019). Light-dependent calcification in Red Sea giant clam *Tridacna maxima*. *Biogeosciences*, 16(13), 2635–2650. <https://doi.org/10.5194/bg-16-2635-2019>
- Sano, Y., Kobayashi, S., Shirai, K., Takahata, N., Matsumoto, K., Watanabe, T., et al. (2012). Past daily light cycle recorded in the strontium/calcium ratios of giant clam shells. *Nature Communications*, 3(1), 761. <https://doi.org/10.1038/ncomms1763>
- Sano, Y., Okumura, T., Murakami-Sugihara, N., Tanaka, K., Kagoshima, T., Ishida, A., et al. (2021). Influence of normal tide and the Great Tsunami as recorded through hourly-resolution micro-analysis of a mussel shell. *Scientific Reports*, 11(1), 19874. <https://doi.org/10.1038/s41598-021-99361-2>
- Schleinkofer, N., Evans, D., Wisshak, M., Büscher, J. V., Fiebig, J., Freiwald, A., et al. (2021). Host-influenced geochemical signature in the parasitic foraminifera *Hyrrokin sarcophaga*. *Biogeosciences*, 18(16), 4733–4753. <https://doi.org/10.5194/bg-18-4733-2021>
- Schmidt, G. A., Annan, J. D., Bartlein, P. J., Cook, B. I., Guilyardi, E., Hargreaves, J. C., et al. (2014). Using palaeo-climate comparisons to constrain future projections in CMIP5. *Climate of the Past*, 10(1), 221–250. <https://doi.org/10.5194/cp-10-221-2014>
- Schöne, B. R., Dunca, E., Fiebig, J., & Pfeiffer, M. (2005). Mutvei's solution: An ideal agent for resolving microgrowth structures of biogenic carbonates. *Palaeogeography, Palaeoclimatology, Palaeoecology*, 228(1–2), 149–166. <https://doi.org/10.1016/j.palaeo.2005.03.054>
- Schöne, B. R., Radermacher, P., Zhang, Z., & Jacob, D. E. (2013). Crystal fabrics and element impurities (Sr/Ca, Mg/Ca, and Ba/Ca) in shells of *Arctica islandica* – Implications for paleoclimate reconstructions. *Palaeogeography, Palaeoclimatology, Palaeoecology*, 373, 50–59. <https://doi.org/10.1016/j.palaeo.2011.05.013>
- Schöne, B. R., Zhang, Z., Jacob, D., Gillikin, D. P., Tütken, T., Garbe-Schönberg, D., et al. (2010). Effect of organic matrices on the determination of the trace element chemistry (Mg, Sr, Mg/Ca, Sr/Ca) of aragonitic bivalve shells (*Arctica islandica*) – Comparison of ICP-OES and LA-ICP-MS data. *Geochemical Journal*, 44(1), 23–37. <https://doi.org/10.2343/geochemj.1.0045>
- Seabold, S., & Perktold, J. (2010). Statsmodels: Econometric and statistical modeling with Python. In *Proceedings of the Python in Science Conferences* (pp. 92–96). <https://doi.org/10.25080/Majora-92bf1922-011>
- Spero, H. J., Eggins, S. M., Russell, A. D., Vetter, L., Kilburn, M. R., & Hönisch, B. (2015). Timing and mechanism for intratest Mg/Ca variability in a living planktic foraminifer. *Earth and Planetary Science Letters*, 409, 32–42. <https://doi.org/10.1016/j.epsl.2014.10.030>
- Tierney, J. E., Poulsen, C. J., Montañez, I. P., Bhattacharya, T., Feng, R., Ford, H. L., et al. (2020). Past climates inform our future. *Science*, 370(6517), eaay3701. <https://doi.org/10.1126/science.aay3701>
- Torrence, C., & Compo, G. P. (1998). A practical guide to wavelet analysis. *Bulletin of the American Meteorological Society*, 79(1), 61–78. [https://doi.org/10.1175/1520-0477\(1998\)079<0061:APGTWA>2.0.CO;2](https://doi.org/10.1175/1520-0477(1998)079<0061:APGTWA>2.0.CO;2)
- Warter, V., Erez, J., & Müller, W. (2018). Environmental and physiological controls on daily trace element incorporation in *Tridacna crocea* from combined laboratory culturing and ultra-high resolution LA-ICP-MS analysis. *Palaeogeography, Palaeoclimatology, Palaeoecology*, 496, 32–47. <https://doi.org/10.1016/j.palaeo.2017.12.038>

- Warter, V., & Müller, W. (2017). Daily growth and tidal rhythms in Miocene and modern giant clams revealed via ultra-high resolution LA-ICPMS analysis—A novel methodological approach towards improved sclerochemistry. *Palaeogeography, Palaeoclimatology, Palaeoecology*, *465*, 362–375. <https://doi.org/10.1016/j.palaeo.2016.03.019>
- Warter, V., Müller, W., Wesselingh, F. P., Todd, J. A., & Renema, W. (2015). Late Miocene seasonal to subdecadal climate variability in the Indo-West Pacific (East Kalimantan, Indonesia) preserved in giant clams. *Palaaios*, *30*(1), 66–82. <https://doi.org/10.2110/palo.2013.061>
- Wit, J. C., de Nooijer, L. J., Wolthers, M., & Reichart, G. J. (2013). A novel salinity proxy based on Na incorporation into foraminiferal calcite. *Biogeosciences*, *10*(10), 6375–6387. <https://doi.org/10.5194/bg-10-6375-2013>
- Yan, H., Liu, C., An, Z., Yang, W., Yang, Y., Huang, P., et al. (2020). Extreme weather events recorded by daily to hourly resolution biogeochemical proxies of marine giant clam shells. *Proceedings of the National Academy of Sciences*, *117*(13), 7038–7043. <https://doi.org/10.1073/pnas.1916784117>
- Yan, H., Shao, D., Wang, Y., & Sun, L. (2013). Sr/Ca profile of long-lived *Tridacna gigas* bivalves from South China Sea: A new high-resolution SST proxy. *Geochimica et Cosmochimica Acta*, *112*, 52–65. <https://doi.org/10.1016/j.gca.2013.03.007>
- Zhao, N., Yan, H., Luo, F., Yang, Y., Liu, S., Zhou, P., et al. (2023). Daily growth rate variation in *Tridacna* shells as a record of tropical cyclones in the South China Sea: Palaeoecological implications. *Palaeogeography, Palaeoclimatology, Palaeoecology*, *615*, 111444. <https://doi.org/10.1016/j.palaeo.2023.111444>